3-2021

Robust Scandium Aluminum Nitride MEMS Resonators for L Band Operation in Orbital Environments

Israel W. Dunk

ROBUST SCANDIUM ALUMINUM NITRIDE MEMS RESONATORS FOR L BAND OPERATION IN ORBITAL ENVIRONMENTS

THESIS

Israel W Dunk, Flight Lieutenant, RAAF

AFIT-ENG-MS-21-M-029

DEPARTMENT OF THE AIR FORCE
AIR UNIVERSITY

AIR FORCE INSTITUTE OF TECHNOLOGY

Wright-Patterson Air Force Base, Ohio

AFIT-ENG-MS-21-M-029

ROBUST SCANDIUM ALUMINUM NITRIDE MEMS RESONATORS FOR L BAND OPERATION IN ORBITAL ENVIRONMENTS

THESIS

Presented to the Faculty

Department of Electrical and Computer Engineering

Graduate School of Engineering and Management

Air Force Institute of Technology

Air University

Air Education and Training Command

in Partial Fulfillment of the Requirements for the

Degree of Master of Science in Electrical Engineering

Israel W Dunk, B.S.E.E.

Flight Lieutenant, RAAF

March 25, 2021

AFIT-ENG-MS-21-M-029

ROBUST SCANDIUM ALUMINUM NITRIDE MEMS RESONATORS FOR L BAND OPERATION IN ORBITAL ENVIRONMENTS

THESIS

Israel W Dunk, B.S.E.E.
Flight Lieutenant, RAAF

Committee Membership:

Matthew Vincie, Ph.D
Chair

Hengky Chandrahalim, Ph.D
Member

Amber Reed, Ph.D
Member

AFIT-ENG-MS-21-M-029

Abstract

This thesis investigates a new combination of aluminum nitride (AlN) alloyed with scandium in a variety of resonator architectures including width extensional mode (WEM), overtone WEM, length extensional mode (LEM), and surface acoustic wave (SAW) that have the potential to achieve high levels of electrical performance and environmental robustness. SAW resonators operating near 370 MHz are fabricated on polycrystalline 37% scandium aluminum nitride ($Sc_{.37}Al_{.63}N$), and AlN with the resulting devices compared and conclusions drawn as to the merits of each material. The design and fabrication of SAW devices is discussed in detail, with the operating characteristics of these resonators then tested both electrically and mechanically, with applications in roles such as satellite communications explored as a possible use case for these devices. Mechanical characterisation includes analysis of vibration and shock effects on the fabricated devices. The electrical characterisation in this work studies the electrical equivalent parameters of the resonators produced. A study is also made into the feasibility of resonant frequency tuning for scandium aluminum nitride ($Sc_XAl_{1-X}N$) SAW resonators using DC bias voltages. Furthermore this work investigates molybdenum and titanium nitride (TiN) as possible candidates for high temperature electrode materials for microelectromechanical systems (MEMS) resonators. Issues encountered during the fabrication of released standing wave devices are also covered with a view to inform potential future works in this area. The devices produced in this work show the future potential for $Sc_XAl_{1-X}N$ piezoelectric materials to produce MEMS resonators operating at high frequencies, at or above 2 GHz with high resilience to shocks, external electric fields and vibrations.

Table of Contents

Page

List of Figures

Figure Page

List of Tables

Table Page

ROBUST SCANDIUM ALUMINUM NITRIDE MEMS RESONATORS FOR L BAND OPERATION IN ORBITAL ENVIRONMENTS

I. Introduction

1.1 Problem Background

The exceptional performance characteristics of radio frequency (RF) microelectromechanical systems (MEMS) resonators and filters have lead to their integration into a vast array of systems [1–3], with RF filtering applications being a dominant area [4]. However, the operation of RF MEMS filters at frequencies approaching 1 GHz and higher remains problematic due to a number of undesirable interactions within the devices that limit performance at and above these frequency ranges [5]. Within radio communications there is currently a drive for higher bandwidth and carrier frequencies in order to increase data transmission rates and escape congestion at lower frequency bands, RF MEMS has faced restricted uptake at these higher frequencies as a result of these limitations [6]. The robustness and suitability of RF MEMS resonators also remains to be fully characterised in some roles.

Of the two key resonator architectures (i.e. piezoelectric and electrostatic), piezoelectric MEMS resonators offer greater promise of achieving high electrical and mechanical performance in the GHz frequency range due to fundamental limitation of the alternative, electrostatically transduced MEMS resonators. These limitation namely being high insertion loss, low transduction efficiency, aggressive feature scaling required to increase transduction efficiency and operate at high frequencies [7], and high bias voltage requirements. Parasitic effects such as feed through, air damping,

and thermo-elastic damping also dominate electrostatic resonators at higher frequencies [5]. Whilst electrostatic resonators typically achieve exceptionally high quality factors and acceptable losses at low frequencies, this performance degrades far faster at higher frequencies than their piezoelectric alternative. This typically results in electrostatic resonators being more suited as filters and frequency references at low frequencies and as high frequency references through frequency multiplication. Piezoelectric MEMS filters on the other hand, have the potential to operate at higher frequencies if sufficiently low losses can be achieved.

In order to increase the range of frequencies at which piezoelectric resonators can operate with acceptably low losses, there is a need to develop new resonator designs and investigate new materials to overcome performance limitations. Whilst some high performance material candidates do exist such as lead zirconate titanate (PZT), environmental and manufacturing considerations surrounding the use of elements such as lead in these materials severely limit their usage [8,9]. Furthermore, for operation in harsh environments such as space, methodologies for testing the robustness of these devices to the unique operating stresses found in space are required.

1.2 Research Objectives

This research investigates options for robust, tunable L Band RF MEMS resonators with center frequencies near 2 GHz having potential applications in the navigation payloads of the next-generation GPS satellites. To achieve this, an emerging piezoelectric material, scandium aluminum nitride, is applied to a variety of existing resonator designs such as length extensional mode (LEM), width extensional mode (WEM), overtone WEM, and surface acoustic wave (SAW).

This work predominately investigates the application of WEM, overtone WEM, and SAW devices to this problem. SAW devices were initially investigated by this

work due to their proven high Q factor and low losses. Additionally, the unreleased structure of SAW devices makes them an ideal candidate for robustness and temperature stability. However, SAW frequency is typically not tuneable and they occupy a relatively large area compared to other potential designs.

In order to investigate options for a more compact and potentially tuneable design in concert with the SAW designs, standing wave devices such as WEM and LEM resonators were considered. LEM devices are typically very compact and also known to have high Q and low loss. However, at higher frequencies aggressive feature scaling diminishes these benefits and motional impedance increases rapidly. As a result of this, WEM and overtone WEM were considered a more viable option for standing wave devices.

In this work 37% scandium aluminum nitride ($Sc_{.37}Al_{.63}N$) piezoelectric has been chosen due to its high electromechanical transduction efficiency (denoted by the electromechanical coupling coefficient κ^2) between electrical and mechanical energy, when compared to other common piezoelectric materials utilized in thin film piezoelectric on silicon (TPoS) resonators; such as aluminum nitride and zinc oxide. Furthermore this material is CMOS compatible and non-toxic, unlike PZT [8, 10]. Increasing κ^2 has the effect of reducing device insertion losses allowing for more efficient operation of these resonators at higher frequencies. And potentially enabling them to operate as front end filters without the need for pre-amplification.

This work also investigates titanium nitride (TiN) and molybdenum as possible candidates for high temperature electrode materials. The high melting point of these material may allow for resonator operation from 1000-1200°C when used as electrode materials [9], far higher than other common electrode materials such as gold or aluminum.

The primary research objectives of this thesis are:

- Systematically characterise the performance, and processing of $Sc_{.37}Al_{.63}N$ thin films as it relates to the resonators developed in this work. Then utilise these results to inform the design and manufacture of robust RF MEMS resonators suitable for high frequency operation. Techniques used include scanning electron microscope (SEM), X-Ray diffraction (XRD), surface profilometetry, and equivalent circuit analysis.

- Design and manufacture a working RF MEMS resonator operating as close to 2 GHz as possible using $Sc_{.37}Al_{.63}N$ thin films as the piezoelectric transducer and characterise the device performance including quality factor, insertion loss, bandwidth, and frequency tunability. Present workable options for resonator designs.

- Determine the suitability of selected resonators for deployment into an orbital environment through environmental testing. This will be characterised by resilience to the shock/vibration of launch and the extremes of temperature experienced in space.

- Investigate the viability of molybdenum and TiN as possible high temperature electrode materials for MEMS resonators.

- Investigate the feasibility of frequency tuning for $Sc_{.37}Al_{.63}N$ films using DC biasing.

- Contrast the results for $Sc_{.37}Al_{.63}N$ against other devices and draw conclusion as to the performance of $Sc_{.37}Al_{.63}N$ in MEMS resonators and suggest possible future work.

1.3 Research Contributions

This thesis contributes to the field of RF MEMS resonators by providing a practical device architecture for future SAW resonators operating near 2 GHz with low insertion loss utilizing poly and single-crystal scandium aluminum nitride ($Sc_X Al_{1-X} N$) piezoelectric material. This is achieved with high quality factor and low insertion loss. The response of these resonators to external vibrations has also been demonstrated experimentally and should inform future design decisions regarding the suitability of these resonators for use in high vibration environments. It is also believed that these devices have the potential to be implemented at a range of frequency bands limited primarily by lithographic constraints.

1.4 Thesis Overview

This thesis is subdivided into six chapters. Chapter two covers the requisite background knowledge for this work and a review of literature in several key related areas. Chapter 3 discusses the design and fabrication work completed in the course of this thesis. The testing methodology employed to characterise the performing of the devices developed in this work is provided in Chapter 4. Results from the testing conducted in this work including etch characterisations, resonator characterisation and material characterisation are related in Chapter 5. Finally Chapter 6 concludes this thesis summarising the key findings and discussing possible future work.

II. Background and Literature Review

This chapter establishes the requisite background knowledge for further discussion of the piezoelectric resonators developed in this work. It first covers general principles of MEMS resonators and Quality factor. Next, possible high temperature electrode materials and the theory of piezoelectric materials with techniques for the characterisation of the piezoelectric films are presented. DC frequency tuning is discussed as it relates to the devices presented in this work. A study of the vibrational characteristics of launch and orbital environments is made in order to inform later vibrational testing. Finally, related research in the field of piezoelectric MEMS resonators is presented to establish the current State-Of-The-Art in this field with a particular focus on emerging $Sc_X Al_{1-X} N$ devices.

2.1 Theory of Operation for MEMS Resonators

Radio frequency microelectromechanical systems (MEMS) resonators have extensive applications in electronics. Perhaps the most influential however are as frequency references and gyroscopes. Each of these applications exploit the resonance of a bulk material at or near it's fundamental mode; or some integer multiple of that frequency for overtone resonators. Signal filtering is achieved in MEMS resonators through the transduction of electrical signals into a variety mechanical waves within the resonator; for example surface acoustic waves, bulk acoustic waves, Lamb waves, and shear waves [1–3, 11].

These waves are characterised by a wavelength given by the frequency of the signal transduced and the acoustic velocity of the material (e.g. 8500 m/s for silicon). For a given material the acoustic velocity is expressed as the relationship between the material acoustic velocity ν_a, acoustic wave frequency f and wavelength λ:

$$\lambda = \frac{\nu_a}{f} \tag{1}$$

As a direct result of the typically far lower acoustic velocity of acoustic waves as compared to the speed of light, these resonators can be realise at an extremely small scales for a given electromagnetic frequency when compared to the wavelength of the same signal in a vacuum. This allows for a significant size reduction when compared to traditional cavity or waveguide filters [6]. Acoustic wave velocities in solids on the order of $1000 - 10,000 m/s$ are common.

The first fundamental resonant mode for bulk mechanical resonators can be approximated by [12]:

$$f_0 = \frac{1}{2\pi}\sqrt{\frac{k_{eff}}{m_{eff}}} \tag{2}$$

Where f_0 is the fundamental mode of the resonator, k_{eff} is the effective stiffness of the resonator and m_{eff} is the effective mass of the resonator. This first mode is the first resonant frequency of the device and typically excites the greatest amplitude of vibration in mechanical resonators. However, overtone modes can also be exploited at integer multiples of the fundamental frequency f_0 [4, 6, 13, 14].

As this wave moves through the resonator structure it can be transduced back into an electrical signal. Frequencies above or below the point of resonance (or an integer multiple of the fundamental frequency) experience significantly lower acoustic admittance and are thus cut off at some $-3\ dB$ bandwidth dependant on device design. In this way, radio frequency (RF) MEMS resonators can form a band pass filter.

The specific wave modes transduced, and the means of transduction play a significant role in the performance of the resonator. The performance of RF MEMS resonators is most often characterised by the following parameters:

- Parasitic feed-through capacitance C_0 — sets the maximum operational frequency of a MEMS resonator. This value is typically small, on the order of $1 \times 10^{-15}F$ or less. However, at sufficiently high frequencies this capacitance will result in significant leakage [15], thus limiting the upper frequency range of MEMS resonators.

- Frequency tunability — the ability, or lack-there-of, for the center frequency of a MEMS resonator, f_0 to be tuned to some other frequency. Multiple techniques have been presented to achieve this, including stiffness tuning, electrostatic tuning, and polarisation tuning [12, 16, 17].

- Bandwidth (f_B) — the maximum continuous $-3\ dB$ bandwidth of the resonator. This is extremely dependant on the individual resonator design, the materials used, and the resonator configuration.

- Quality (Q) factor — a term used to describe the ratio of energy stored to energy dissipated within the resonator. Defined as $Q = f_0/f_B$ where f_0 is the center frequency of the resonator and f_B is the $-3\ dB$ bandwidth. A higher Q indicates a less damped resonator. A discussion of the damping mechanisms affecting the Quality factor of MEMS resonators is provided in Section 2.1.1.

- The figure of merit (FOM) — a term used to quantitatively compare resonator performance, defined as $FOM = f_0 \times Q$. This term is often a more meaningful way to describe resonator/filter performance; whilst Q is related to device losses, it is also tied to the device operating frequency and bandwidth. This makes a comparison between devices with different pass-band characteristic and

operating frequencies less meaningful. FOM can fill this gap as a more absolute measurement of device performance taking into account device losses and operating frequency. The theoretical upper limit of possible FOM for a given material is typically set by Akhiezer damping [5, 7, 18, 19] and is referred to as the Akhiezer limit of a material in this context.

- Motional impedance — the electrical equivalent resistance of the resonator R_m. This is strongly influenced by the Q factor of the resonator. Resonator insertion loss is inversely proportional to Q, thus it is typically beneficial to maximise Q in order to minimise insertion loss.

2.1.1 Resonator Quality Factor

The quality factor of an RF MEMS resonator is influenced by the combined interactions of a number damping mechanism. The total effect of these mechanism can be expressed as [7]:

$$\frac{1}{Q} = \frac{1}{Q_{AKE}} + \frac{1}{Q_{TED,Bulk}} + \frac{1}{Q_{ANC}} + \frac{1}{Q_{SURF}} + \frac{1}{Q_{AIR}} \tag{3}$$

Akhiezer damping Q_{AKE} describes damping resulting from the scattering of momentum carrying phonons within the crystal structure of a material. This damping mechanism posses a theoretical upper limit to the FOM of a resonator based purely on it's material composition due to the damping force increasing rapidly with the operating frequency [5, 7]. This means that the product $FOM = f_0 \times Q$ cannot be increased past a certain upper limit governed by the materials used in a given resonator. This is a result of a rapid decrease in Q in response to very high frequencies. Typically this limit is within several orders of magnitude of $FOM = 10^{13}$ [5].

Losses within the bulk material from thermoelastic damping are described by $Q_{TED,Bulk}$. This results from energy dissipated as thermal energy when crystal bound-

aries and lattice defects shift past one another. This is typically lower for single crystal materials due to the far lower instances of crystal boundaries and latices defects.

Surface losses are given by Q_{SURF} and result from imperfections in the surface of a resonator.There are multiple source for surface damping, including micro-cracks and minute amounts of trapped gases within the surface layers of a device.

Anchor losses Q_{ANC} result from the loss of acoustic energy within the resonator when it is radiated out in to the bulk substrate either through either the resonator tethers, or through the mounting point of the resonator to the substrate for solidly mounted resonators such as surface acoustic wave (SAW) and bulk acoustic wave (BAW) resonators. Anchor loss can be minimised through anchor design and the inclusions of acoustic reflectors such as Bragg reflectors or phononic crystals. These structures reflect a fraction of the acoustic energy back into the the resonator. Well designed reflectors can approach unity reflectivity and thus significantly increase the quality factor of the resonator.

A common method of minimising loss through tethers is to have anchor lengths of $\lambda/4$, where λ is the wavelength of the resonator center frequency f_0. This makes the anchors substantially stiffer than the resonator body and reduces the acoustic admittance of the anchors to the resonant wavelengths. Alternative anchor designs to minimise anchor losses are presented in several works such as *Anchor Design Affects Dominant Energy Loss Mechanism in a Lamé Mode MEMS Resonator* by Gabrielle D. Vukasin et al. [18]. The inclusion of reflectors and phononic crystals have also been employed to reduce anchor losses [20].

Interactions between the surface and the atmosphere surrounding the resonator result in viscous damping, describe by Q_{AIR}. Energy is dissipated via the transfer of kinetic energy to the surrounding air. Resonator design and operation at reduced pressure can minimise the effects of viscous-damping.

2.1.2 Common Transduction Methods for MEMS Resonators

There are two dominant methods for signal transduction in MEMS resonators, these are electrostatic and piezoelectric transduction. In an electrostatic resonator the resonator body is driven by the force of an electric field across a capacitive gap. For a two port device, the resulting acoustic waves can then be transduced across a second capacitive gap back into an electrical signal. These resonators are typified by very high Q factors but also high motional impedance due to the relatively low transduction efficiency of this method. This low transduction efficiency yields a high equivalent circuit impedance R_m for the resonator. In general, extremely small capacitive gaps are required in electrostatic resonators to achieve low values for resonator motional impedance and thus low insertion losses [7, 19, 21].

Capacitive gaps less than 100 nm are considered excellent. However, far smaller values may be required to achieve motional impedance values close to 50Ω. Such small gaps may not be practical or possible to manufacture, thus placing a hard limit on the minimum resonator impedance. This makes impedance matching electrostatic devices to high frequency RF circuits problematic. Matching networks can be employed to overcome impedance matching issues, but typically introduce additional phase noise, power consumption and overall complexity. This makes system integration of electrostatic resonators for RF systems problematic and illustrates that it is desirable to have input impedance values for MEMS resonators near 50Ω to avoid the need for matching networks. A common example of an electrostatically transduced resonator is the ubiquitous electrostatic comb drive resonator shown at Figure 1. Here the electrostatic transduction is achieved at the input and output of the device through the use of two pairs of interdigitated combs. The center shuttle of the resonator is freely sprung using a folded spring type suspension. The shuttle oscillates when driven by an input signal, with the greatest amplitude experienced when driven at resonance.

DC biasing of the comb structure is required in this case to generate an electric field within the moving comb. The moving shuttle, with its DC bias voltage, moves the output comb fingers relative to each other, resulting in a signal at the output directly proportional to the frequency of oscillation of the shuttle. Input and output ports have not been marked in Figure 1 as the device shown operates identically in both directions regardless of the choice of input and output ports.

In contrast to electrostatic devices, piezoelectric resonators exploit the piezoelectric effect to excite a resonator. In this case a suitable piezoelectric material is directly coupled to a bulk resonator body, or used as the bulk resonator itself with one or more sets electrodes attached (one-port, two port, or N port resonators being possible). For a two port device, the input RF signal is fed in from the input electrode, the result-

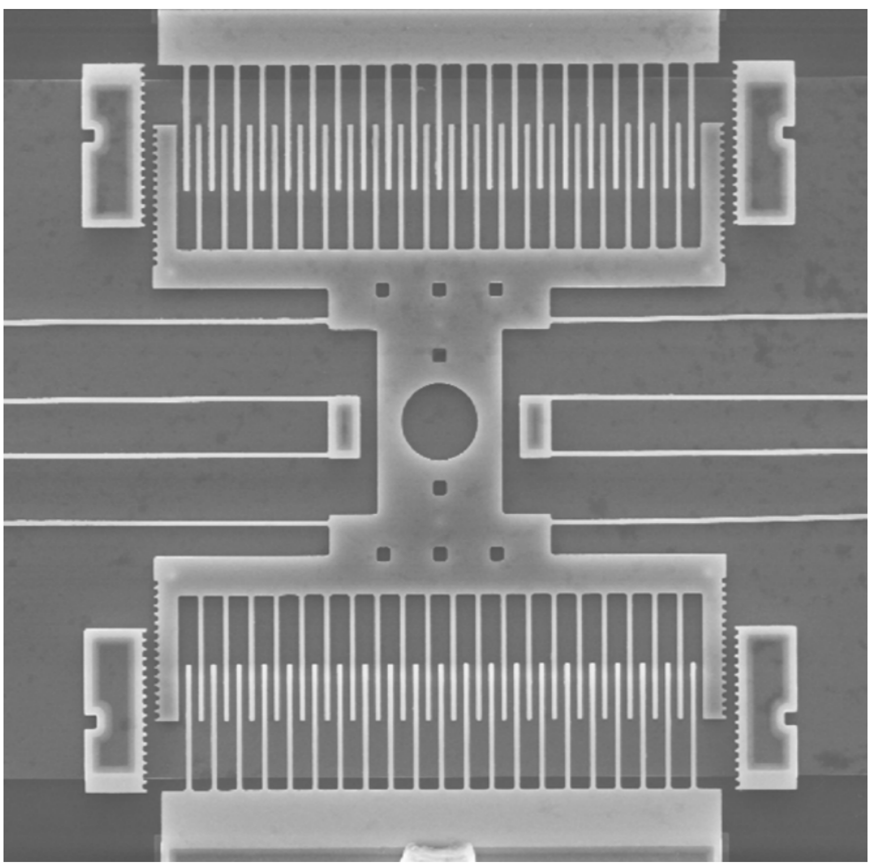

Figure 1: Example of the ubiquitous electrostatic comb-drive resonator [22]

ing electric field between the electrode and a grounding plane generates a stress field within the piezoelectric material [23]. As the field varies in polarity with time, expansion and contraction of the piezoelectric film results, establishing a mechanical wave within the body of the resonator.

Resonators can be of two typical transduction types: either signal port or multi-port. Figure 2 illustrates a one and two port piezoelectric resonator. Single port devices maximise the transduction area via the use of the entire device area for transduction. These devices have applications as frequency references but cannot pass a signal through. Thus they cannot be used as band pass filters.

Multi port devices sacrifice some transduction area in order to allow for two or more transduction electrodes. This allows for a signal to be passed through the resonator. These devices have applications as frequency references but also as band pass filters.

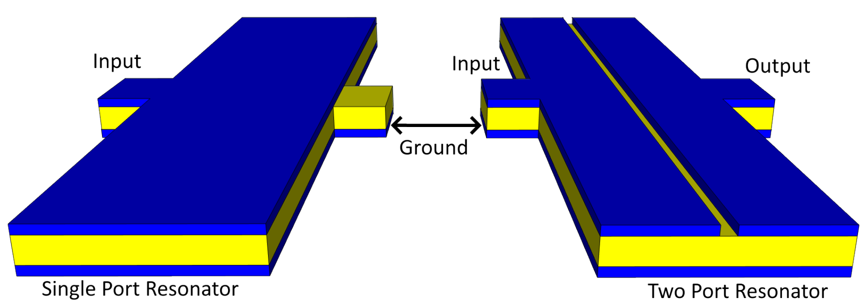

Figure 2: Illustration of one port (left) and two port (right) standing wave piezoelectric length extensional mode resonator. Piezoelectric material is in yellow and metal electrodes are in blue. The top electrodes serves as the input and output as applicable. The bottom electrode is the ground plane for the device.

2.2 High Temperature Electrode Materials

The identification of suitable high temperature electrode materials will allow for the operation of RF MEMS resonators in very high temperature environments. Molybdenum and titanium nitride are two possible candidates investigated in this work. These materials typically show sheet resistances on the order of those shown in Table 1. These are presented alongside sheet resistance measurements of other common electrode materials.

Table 1: Selected sheet resistances for common MEMS electrode materials and proposed high temperature electrode materials

Material	**Resistance** ($\Omega/\square$)
Molybdenum	$\approx 1 - 10$ [24]
Titanium Nitride	$\approx 70 - 160$ [25]
Gold	0.48
Aluminum	0.56
Copper	0.34

As shown, molybdenum compares favorably with more traditional electrode materials. However, titanium nitride (TiN) typically has higher sheet resistance which may limit it's use. It is desirable to utilise TiN however as higher quality films of scandium aluminum nitride ($Sc_XAl_{1-X}N$) can be grown on TiN layers. Attempts have been made by external collaborators to deposit TiN with lower resistivity, which this work will aim to characterise these films to determine their suitability.

Regarding molybdenum, recent works report that whilst thick films of molybdenum typically show acceptably low sheet resistance values, this increases rapidly in thin films on the order of $100nm$ or less [24]. This may be a limiting factor in the development of certain resonator architectures such as SAW where the mass loading of the electrodes is an important consideration, thus desirable to operate with very thin electrodes. Furthermore the sheet resistance of Mo thin films has been shown

to be strongly dependant on the sputtering conditions [24, 26, 27]. This may pose a hard limit on the achievable sheet resistance values in this work due to limitation of the equipment available.

2.3 Piezoelectric Theory

The properties of piezoelectrically transduced resonators are strongly determined by the piezoelectric coefficients of the materials used in the device. The piezoelectric coefficients d_{iq} and e_{iq} describe the conversion in a material between electrical and mechanical forces. The higher this conversion factor, the more efficiently energy can be transferred through the resonator. When looking at a MEMS resonator as a whole, this efficiency is combined with other terms to yield the electromechanical coupling coefficient κ^2. Typically κ^2 is derived from experimental measurement of the electrical characteristics of a resonator, as it is dependant on the specific properties of a given device.

The piezoelectric coefficients of a material are expressed as a coupling between between the mechanical elastic variables, stress (T) and strain (S), and the dielectric variables, electric displacement field (D) and electric field (E) [28]. If these properties are considered in terms of the linear theory of piezoelectricity the parameters can be written as a system of linear equations relating each of these properties to the electric displacement field in the i^{th} direction D_i and mechanical stress in the q^{th} direction T_q [23] as shown by [23, 28]:

$$D_i = d_{iq}T_q + \varepsilon^T_{iq}E_q \tag{4}$$

$$T_q = T_e + T_{pe} \tag{5}$$

Where T_e is the elastic stress caused by a force directly on the material and T_{pe} is the additional stress induced by the electric field resulting from the initial deformation stress T_e, the dielectric constant under constant stress for the material is given by the matrix ε_{iq}^{T}, and d_{iq} is the scalar piezoelectric constant relating an applied stress in the i^{th} direction to the field developed in the q^{th} direction.

Focusing on the relationship for the charge displacement within the material (4), useful metrics for the performance of piezoelectric material can then be developed. This relationship is derived as a ratio between the strain applied and the electric field developed in the material (the mechanism by which piezoelectric resonators function). From (4) d_{iq} can be given by either

$$d_{iq} = \frac{Strain\,Applied}{Field\,Developed} \tag{6}$$

or

$$d_{iq} = \frac{Charge\,Density\,at\,Open\,Circuit}{Applied\,Stress} \tag{7}$$

This makes the parameter d_{iq} a useful metric for describing the performance of a piezoelectric materials for use in MEMS resonators as it concisely describes the ability of the material to convert between electrical and mechanical energies. As such it will be referenced throughout this report when discussing piezoelectric materials. The parameter e_{iq} is also often used for the same purpose, as this describes the reciprocal relationship between mechanical and electrical energy. From this one of the key benefits of scandium aluminum nitride can be articulated. Namely that $Sc_XAl_{1-X}N$ films have high d_{iq} and e_{iq} coefficients relative to aluminum nitride (AlN). Furthermore, d_{iq} and e_{iq} have been shown to increase with increasing scandium doping concentrations up to 42% [29–31].

Piezoelectric materials are however, anisotropic and thus the response of a given piezoelectric will vary based on the crystallographic axis of the piezoelectric crystal considered. This is accounted for in the sub-scripting convention, as seen in (4). Figure 3 demonstrate the common coordinate naming system used [23, 28]. By convention, dimension 1 is in the direction of the strain and dimension 2 is orthogonal and in the same crystal plane. Dimension 3 is typically out of the plane and equivalent to the z-axis. Dimensions 4, 5, and 6 are also assigned to represent shear forces and responses. It is important to note that these dimensions primarily represent the directions of forces and responses, not spacial dimensions.

In general the charge displacement in the i^{th} direction will be the result of the combined contributions of the strain in each dimension and the charge displacement imposed by any electric fields, which is dependant on the relative permeability of the material. This can be expressed generally in matrix form as [23]:

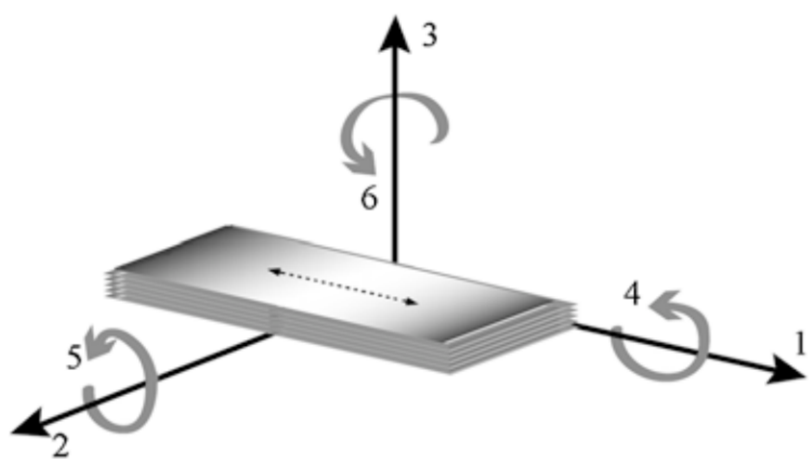

Figure 3: The six common sub-scripted piezoelectric axis' [28]

$$
\begin{bmatrix} D_1 \\ D_2 \\ D_3 \end{bmatrix} = \begin{bmatrix} d_{11} & d_{12} & d_{13} & d_{14} & d_{15} \\ d_{21} & d_{22} & d_{23} & d_{24} & d_{25} \\ d_{31} & d_{32} & d_{33} & d_{34} & d_{35} \end{bmatrix} \begin{bmatrix} T_1 \\ T_2 \\ T_3 \\ T_4 \\ T_5 \\ T_6 \end{bmatrix} + \begin{bmatrix} \varepsilon_{11}^T & \varepsilon_{12}^T & \varepsilon_{13}^T \\ \varepsilon_{21}^T & \varepsilon_{22}^T & \varepsilon_{23}^T \\ \varepsilon_{31}^T & \varepsilon_{32}^T & \varepsilon_{33}^T \end{bmatrix} \begin{bmatrix} E_1 \\ E_2 \\ E_3 \end{bmatrix} \tag{8}
$$

Symmetry in the piezoelectric material, as well as processing conditions will determine which components of the matrix are in fact non-zero. Exploiting these factors can substantially simplify the the matrix.

The properties of piezoelectric films are commonly derived through experimental measurements utilising a number of techniques. Common methods include X-Ray diffraction (XRD), selective area electron diffraction (SAED), laser interferometry, resonant frequency method, and quasi-static method [32].

The orientation dependence of the piezoelectric properties of a material makes the crystallographic orientation of the deposited film highly relevant to device performance. Preferential orientation along an axis of high piezoelectric coefficient will substantially improve the performance of a resonator. Existing research shows that for a Wurtzite crystal structure such as that seen in $Sc_X Al_{1-X} N$ the piezoelectric coefficient along the C-Axis of the material corresponding to the $\{0001\}$ crystallographic axis is most desirable as this axis shows the greatest piezoelectric response [31,33,34].

The exploitation of multiple acoustic modes in a MEMS resonator can be used to achieve higher total coupling efficiency κ^2 via the combination of piezoelectric forces along multiple films axis' to achieve an overall higher effective κ^2. For example, Guofeng Chen and Matteo Rinaldi exploit this effect in *Aluminum Nitride Combined*

Overtone Resonators for the 5G High Frequency Bands [35] to couple the response from the e_{33} and e_{15} coefficients to achieve a higher κ^2 than could be achieved using by either coefficient alone.

Multiple coupled modes can also be exploited for frequency tuning of MEMS resonators whose architectures would not typically allow for this. Frequency tuning of thickness mode resonators using in plane dimensions is shown by several authors [12, 35].

2.4 DC Frequency Tuning Theory

DC frequency tuning of MEMS resonators has been presented in a number of recent works [12, 17]. Typically frequency tuning is achieve via the use of a DC bias to impart a strain or pre-load upon the resonator body in order to modify it's stiffness. As we have seen in (2) the resonant frequency of a mechanical resonator is directly related to the resonator stiffness.

In thin film piezoelectric on silicon (TPOS) resonators, frequency tuning is also achievable via modification of the piezoelectric coefficients in ferroelectric materials. Ferroelectric materials can be polarised by the application of an external DC field in order to display piezoelectric properties. Such materials are only piezoelectric when polarised. The strength of this polarisation is proportional to the field applied. The polarisation of non-ferroelectric piezoelectric materials can also be influenced by an external DC field. The devices presented in this work attempt to exploit a change in the polarisation of the $Sc_XAl_{1-X}N$ film in order to realise DC frequency tuning of the devices.

2.5 Vibrational Characteristics of Orbit and Launch

The launch of systems into orbit and orbital environments pose unique vibrational conditions not typical of many other environments that MEMS devices might be employed in. Furthermore, the very nature of MEMS resonators as acoustic devices makes them potentially susceptible to the strong vibrations and shocks common in these environments.

To determine the suitability of the resonators presented in this work for deployment in such environments, it is essential to characterise both the expected vibrational environment and the response of the resonators developed in this work to those vibrations.

A review of relevant literature in this area has been conducted to inform this process and suggest regions where the greatest intensity of vibration can be expected. Extensive work by National Air and Space Agency (NASA) provides insight into the vibrational environments of several legacy space launch platforms such as the Titan and Saturn systems [36, 37]. These references indicate that the strongest vibrations can be expected from $1 - 2000\ Hz$ with particularly strong vibrations between $1 - 1000\ Hz$.

2.6 Related Research

2.6.1 RF MEMS for Space Based Applications

Research by Roberto Sorrentino et al. has investigated the application of RF MEMS switches and resonators to space based applications as a low size and weight alternative for reconfigurable waveguides within these platforms, showing equivalent or better performance characteristics to existing cavity and waveguide filters. How-

ever, no mention of the suitability of these devices regarding environmental robustness is made [4].

The effects of thermal and mechanical cycling on RF MEMS switches for applications in space based systems are investigated in *Reliable response of RF MEMS Low Temperature Co-Fired Ceramic (LTCC) packaged switches after mechanical and thermal stress* [38]. In this work it was found that the response to mechanical vibrations of the MEMS devices was quite acceptable. However thermal cycling was determined by the authors to be the more limiting factor on system life due to thermal stress within thin wide regions of the device used for component suspension. This resulted in creep, bucking, and cracking of these elements after repeated cycling.

2.6.2 Properties of Scandium Aluminum Nitride

Thin films of $Sc_X Al_{1-X} N$ have been demonstrate in multiple recent works to substantially improve the performance of TPoS resonators as a result of its larger piezoelectric coefficients [9, 29, 30, 39–42]. Experimental results by Stefan Mertin et al. [29, 30] characterised the piezoelectric coefficients for $Sc_X Al_{1-X} N$ at a variety of scandium doping concentrations. This study primarily focused on the d_{33} and e_{31} coefficient for $Sc_X Al_{1-X} N$ thin films. In their work it was shown that the magnitude of the piezoelectric coefficients increased with increasing scandium doping up to the tested limit of 35%. The authors observed an e_{31} of $-2.67C/m^2$ which is approximately 2.5 times higher than that of an equivalent AlN thin film. The d_{33} coefficient was maximised at 35% scandium doping with a value of $10.2pm/V$. However, for the piezoelectric coefficients investigated in this work, the maximum values reported were found at the maximum doping concentration tested. Thus higher doping concentrations may increase piezoelectric coefficient values further.

The authors also noted possible issues with crystal growth at higher values of scandium doping. The authors attribute this primarily to film stress caused by the scandium dopant. This resulted in abnormal grain growth, with the C-axis of the lattice not aligned perfectly in the desired direction of growth.

Further research regarding the adverse affects of scandium doping percentages in AlN films is presented by Chen Liu et al. in their paper titled *Evaluation of the Impact of Abnormally Orientated Grains on the Performance of ScAlN-based Laterally Coupled Alternating Thickness (LCAT) Mode Resonators and Lamb Wave Mode Resonators*. Here the authors evaluate the incidence of abnormal grain growth in $Sc_X Al_{1-X} N$ when correlated with the scandium doping concentration. This work concludes that increased scandium doping increases films stress and the density of abnormally oriented grains within the film. This work also concludes that the abnormally oriented grains result in a variation in the piezoelectric coefficients, and dependant on the axis considered, either an increase or reduction in the piezoelectric coefficients observed.

Similar results for the piezoelectric coefficients were shown in an earlier work by Miguel A Caro et al. [31] whom also worked to provide an extensive characterisation of thin films of $Sc_X Al_{1-X} N$ up to 50% scandium doping in BAW resonators. However they do not contrast this against the performance of a similar AlN resonator.

These results are further supported by the recent results from Roy H. Olsson , Zichen Tang, and Michael D'Agati in their paper titled *"Doping of Aluminum Nitride and the Impact on Thin Film Piezoelectric and Ferroelectric Device Performance"* [43]. This report provides an extensive comparison of the properties of AlN and $Sc_X Al_{1-X} N$ films. Their results, whilst showing some experimental variation meet or even exceed the values for piezoelectric coefficient shown in previous works. For example the d_{33} coefficient is shown to achieve values of approximately $23pm/V$

at approximately 34% scandium doping. However, the authors also provide a very detailed analysis of some of the detrimental effects of increased scandium doping not discussed in depth in previous works. This includes a steady reduction in elastic modulus and an increase in relative permittivity. This results in decreasing acoustic velocity in the the piezoelectric material. However, increasing permittivity increases the polarizability of the material boosting electromechanical coupling.

From these works it can be concluded that increasing the scandium doping concentration in AlN films will result in higher piezoelectric coefficients and thus there is strong potential for improved resonator performance when compared to AlN resonators. However, this must be balanced against the possibilities for abnormal grain growth, high film stress, and reductions in stiffness when considering this material for potential resonators.

2.6.3 Recent Developments in MEMS Resonators

Recent developments in the field of RF MEMS resonators have attempted to further increase the capability of these devices by extending the operating frequency into the GHz range though a number of means. In *Aluminum Nitride Combined Overtone Resonators for the 5G High Frequency Bands* Guofeng Chen and Matteo Rinaldi [44] employed multiple overtones simultaneously to achieve a operating frequency of 8.8 Ghz with low insertion losses utilising aluminum nitried TPoS resonators; with aims to potentially reach up to 40 Ghz. This was achieved through the coupling of multiple resonant modes. The use of multiple modes also achieved a higher total effective electromechanical coupling κ^2 though the addition of piezoelectric coefficients from multiple piezoelectric planes.

The potential for on chip integration of $Sc_X Al_{1-X} N$ devices is demonstrated by Afzaal Qamar et al. in *ScAlN/3C-SiC/Si platform for monolithic integration of highly*

sensitive piezoelectric and piezoresistive devices [45]. In this work the authors demonstrate a monotonically integrated platform using $Sc_XAl_{1-X}N$ thin films on both silicon and silicon carbide substrates. In particular, the authors note the benefits of manufacturing $Sc_XAl_{1-X}N$ on SiC substrates due to the reduction in lattice mismatch between between the piezoelectric film and the substrate when compared to pure silicon. This markedly improved the grain growth and uniformity of the grown $Sc_XAl_{1-X}N$ resulting in increased device performance. The authors also performed measurements on a SAW resonator with a center frequency of 2.73 Ghz as an element of the characterisation process. This showed an insertion loss of -30 dB and stop band attenuation of -18 dB. This clearly demonstrates an improvement in device performance at these frequencies when compared to similar AlN devices. However there is still substantial room for improvement in this space, both in terms of reducing insertion loss and increasing stop band attenuation. Furthermore this work illustrate the benefits of piezoelectric growth on preferential substrates such as TiN.

A record Q of $23.2K$ was achieved by Sarah Shahraini in a thickness Lamé TPoS resonator utilising $Sc_XAl_{1-X}N$ thin film as the transducer and the constructive combination of the d_{31} and d_{33} piezoelectric coefficient to boost the overall electromechanical coupling [46]. A low motional impedance of 235Ω is also achieved in this design. This exemplifies the improved electromechanial coupling coefficient of $Sc_XAl_{1-X}N$ as the motional resistance for Lamé mode resonators is typically impractically high above 100 Mhz. The author however was only able to achieve these results at frequencies of 185 Mhz, far below the frequencies of interest to this work.

Chien-Hao Weng et al. [47] demonstrated in *A Thin-Film Piezoelectric-on-Silicon MEMS Oscillator for Mass Sensing Applications* a low frequency high Q resonator for mass sensing achieving very low phase noise, high sensitivity, and low temperature coefficient of frequency using a PZT TPoS architecture.

Multiple overtone modes are also excitable with electrostatic transduction as shown by Zeji Chen et al. in *A Switchable High-Performance RF-MEMS Resonator with Flexible Frequency Generations* [35]. In this paper they excite the second to seventh overtone mode in an electrostatic resonator achieving Q values of up to 10^4 at frequencies of 366 Mhz. They also achieve exceptionally low motional resistance values for an electrostatic resonator in the range of $765 - 3050\Omega$ with ultra small capacitive gaps of 70 nm. This paper represents a significant level of performance for a very recent electrostatic resonator. However this resonator was not demonstrated to perform satisfactorily at GHz frequencies for front end filtering roles, demonstrating the continuing limitation of electrostatic MEMS resonators.

A Tunable Ferroelectric Based Unreleased RF Resonator from Yanbo He et al. [48] demonstrates a novel fully chip embeddable resonator design, produced with the Texas Instruments Ferroelectric RAM (FeRAM) technology. This work demonstrates ongoing efforts towards fully embedded RF MEMS Resonators.

An extremely high electromechanical coupling of 12% was demonstrated by Nan Wang et al. in their paper titled *Over 12% of Coupling Coefficient Demonstrated by 3 Ghz $Sc_{0.12}Al_{0.88}N$ Based Laterally Coupled Alternating Thickness (LCAT) Mode Resonators* [49]. This further demonstrates the performance of $Sc_XAl_{1-X}N$ as a transducer material. It should be observed however, that this level of coupling will not likely be achievable in practically implemented two-port devices as these results reflect measurements of the S_{11} parameter of a 1-port device only and as such the results are somewhat contrived due to the additional transduction area available to 1-port resonators. However, these do support the measurements made by other authors in terms of S_{11} parameters. Furthermore these result reflect positively on the potential of $Sc_XAl_{1-X}N$ resonators.

Large increases in electromechanical coupling coefficient were also demonstrated in *Scandium Aluminum Nitride-Based Film Bulk Acoustic Resonators* [50]. However, the authors also note a significant decrease in the quality factor of the resonators attributable to the increased damping factor of the $Sc_XAl_{1-X}N$ piezoelectric.

An extremely wideband lateral overtone bulk acoustic resonator (LOBAR) architecture was demonstrated by Ali Kourani et al. in their paper titled *A Wideband Oscillator Exploiting Multiple Resonances in Lithium Niobate MEMS Resonator* [13]. The resonators achieved exceptional bandwidth by exploiting many closely spaced overtone modes between 100 and 800 MHz. This is a somewhat indirect means of achieving this high bandwidth as the bandwidth was not contiguous but instead many discrete frequencies spaced between the upper and lower bandwidth values. This makes these devices less generalised as they do not display continuous frequency tunability; which is a goal of this work.

In *Nano-Precision Deep Reactive Ion Etching of Noncrystalline 4H-SiCOI for Bulk Acoustic Wave Resonators with Ultra-low Dissipation* SiC based electrostatic resonators were demonstrated by J. Yang et al. showing extremely low dissipation and high Akhiezer limit [7].

Low motional impedance distributed Lamé resonators (DLR) were demonstrated by Anosh Daruwalla et al. [19]. These resonators demonstrated extremely high Q values and exceptional temperature stability.

Further applications of $Sc_XAl_{1-X}N$ piezoelectric material is demonstrated by Jialin Wang Et. Al in their paper titled *A Film Bulk Acoustic Resonator Based on Ferroelectric Aluminum Scandium Nitride Films* [51]. Here the frequency tuning ability of $Sc_XAl_{1-X}N$ films are demonstrated experimentally along with polarisation switching. This supports the possibility of DC frequency tuning of $Sc_XAl_{1-X}N$ film based filters. Tuning ranges of 2% are presented. This would indicate a tuning range

of 80 Mhz at 2 Ghz might be achievable. This work also supports the claims of previous works suggesting that scandium doping concentrations above 30% are ideal for piezoelectric MEMS devices due to high piezoelectric coefficient and indicates that concentrations above 27% doping yield improved tuning.

Examples of single crystal epitaxial aluminum scandium nitride resonators are presented by Mingyo Park et al. in their work titled *Epitaxial Aluminum Scandium Nitride Super High Frequency Acoustic Resonators* [52]. The authors exploit 12% scandium aluminum nitride films to produce resonators operating in the $3-10$ Ghz frequency range with potential applications in 4G LTE and 5G. The authors note a low quality factor of 192 and discuss issues experience with excessive film stress in the sub-micron 400 nm piezoelectric film utilised as a potential cause. The authors also note that film stress increases with increasing scandium doping concentration; an important consideration for this research area.

The work titled *Super High Frequency Simple Process Flow Cross-Sectional Lamé Mode Resonators in 20% Scandium-Doped Aluminum Nitride* [53] by Zachary A. Schaffer et al. presents cross sectional lamé resonators using $Sc_XAl_{1-X}N$ films up to 20% scandium concentration. The authors in particular note the benefits of $Sc_XAl_{1-X}N$ films and present a simple process flow for producing these resonators. The resonators developed it this work show Quality factors of around 500 in the frequency range from $3-6$ Ghz.

III. Resonator Design and Fabrication

3.1 Resonator Designs

3.1.1 Piezoelectric Materials Used

Three different piezoelectric materials were used in this work. Poly and single crystalline films of scandium aluminum nitride ($Sc_X Al_{1-X} N$) were chosen to test the effects of high scandium doping concentrations with 30% scandium in the single crystal samples and 37% scandium in the polycrystalline samples. Aluminum nitride was chosen to provide a reference point for the films alloyed with scandium.

3.1.2 SAW Design

One and two port surface acoustic wave (SAW) layouts were developed for two key operating frequencies in this work. SAW resonators typically comprise one or more arrays of interdigital transducers (IDTs) and two or more arrays of acoustic Bragg reflectors which form a resonant cavity to contain surface wave energy; preventing dissipation of the surface wave into the bulk substrate. For a two port SAW resonator the IDTs generate a stress field on the surface of the a substrate that propagates through an acoustic cavity between the input and output transducers.

The resonant frequency of a SAW resonator is set by the pitch of the resonator IDTs and the acoustic velocity of the substrate as given by:

$$f_0 = \frac{\nu_m}{2P} \tag{9}$$

Where f_0 is the first resonant frequency, P is the IDT pitch and ν_m is the acoustic velocity of the metallized substrate. The design of SAW resonators requires careful consideration of a number of critical device dimensions and substrate properties in

order to maximise the performance of the resonator. An annotated diagram for a two port SAW resonator is provided at Figure 4 detailing each of the critical dimensions.

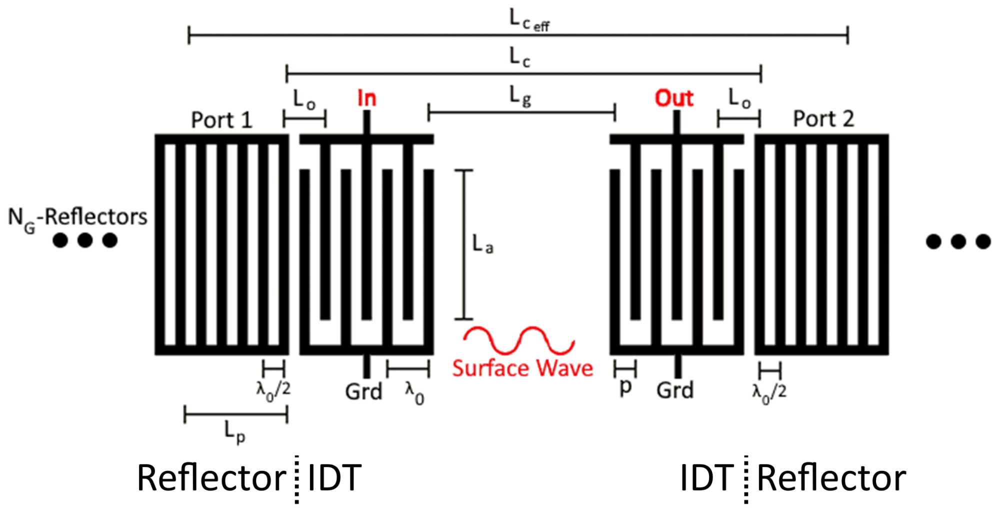

Figure 4: Critical dimensions for SAW resonator design. L_g is the length of the gap between the input and output sides of the resonator. L_c is the length of the resonant cavity between reflector arrays. The pitch of the IDTs, marked as P is equal to $\lambda/2$. The pitch denotes the separation between consecutive ground and signal fingers in the IDTs. The acoustic aperture L_a is the length of interpenetration of the IDT fingers [54]. L_o is the offset of the IDTs from the reflectors. Please note that the proportions in this image have been selectively manipulated for clarity.

The separation between the input and output sides of the resonator, L_g should be an integer multiple of wavelengths. The length of the resonant cavity and positioning of the the input and output transducers must be set such that constructive interference occurs for the IDTs. The length L_o is the offset of the IDTs from center of the first reflector to the center of the IDT finger closest to the reflector. This should be set such that [54]:

$$L_o = N\frac{\lambda}{2} + \frac{3\lambda}{8} \tag{10}$$

Where N is an integer value. This is the requisite condition to ensure that the waves reflected within the cavity interfere constructively with the IDTs. The overall

cavity length should be an integer number of wavelength to form Fabry-Perot cavity. However, true cavity length will be the sum of L_c and $2L_p$, where L_p is the penetration distance of the SAW wave into each reflector bank. As such, each end of the cavity will form at a point within the reflector array, assuming that there are sufficient reflector gratings to approximate unity reflectivity within the cavity. If this is not the case, then SAW energy will leak into the bulk substrate.

The length of the resonant cavity formed by the reflector arrays should be set such that [54]:

$$L_{c_{eff}} = 2L_p + L_c \tag{11}$$

$$L_{c_{eff}} = (n-1)\frac{\lambda_0}{2} \tag{12}$$

Calculation of the cavity length however, is not trivial due to the need to precisely understand the specific material properties of the resonator in order to calculate the penetration depth of the SAW wavefront as given by [54]:

$$L_p = \frac{tanh((N_G-1)r_s)\lambda_0}{4r_s} \tag{13}$$

Where N_G is the number of gratings in a reflector bank and r_s is the acoustic reflectivity at the frequency of interest for a single reflector grating. The reflectivity of a single grating can be given by [54]:

$$r_s = a + b\frac{h}{\lambda_0} \tag{14}$$

Where a and b are material specific parameters that can be determined experimentally. The parameter h is the height of a reflector strip. For the materials used in this work however, these parameters were not known from the outset and thus the required number of reflectors were conservatively estimated from other related

works. By simplifying (15) using the assumption that $N_G \to \infty$ the equation can be expressed as [54]:

$$L_p = \frac{\lambda_0}{4r_s} \tag{15}$$

Putting a conservative lower bonds on the reflectivity per grating of 0.005 results in an estimated penetration depth of 600 μm for $\lambda_0 = 12$ μm, requiring $N_G = 100$ for a reflector pitch of $\lambda_0/2 = 6$ μm. Thus each reflector array should contain somewhat more than $N_G = 100$ reflectors. This estimate of r_s is likely low, but it ensures that the SAW energy is fully contained in the reflector array.

The total length of the acoustic cavity $L_{c_{eff}}$ is also related to the Q factor of the SAW device, with Q rising as the length of the cavity increases [54]. Thus it is typically desirable to maximise the cavity length $L_{c_{eff}}$ to a point. This is analogous to coupling the SAW resonator to a large high Q proof mass. However, excessively long cavities can result in leakage of the acoustic waves into the bulk substrate. Thus designs must balance these factors.

3.1.2.1 Solid and Split Transducer Designs for SAW Resonators

The IDTs of a SAW resonator can be designed as either a solid or split transducer topology. Solid IDTs have reduced lithographic requirements and simplified construction. However, it can be observed that the IDTs also reflect the surface waves traveling through the acoustic cavity in the same manner that the reflector arrays do [54]. This can result in self cancellation of surface waves within the cavity by the reflections from the IDTs.

Splitting the transducers as shown in Figure 5 can resolve this issue at the expense of additional lithographic requirements. In a split IDT design, the periodicity of the transducers strips doubles, but the effective centers of strain for the transduc-

ers remain the same. This means that the reflections from the IDTs now occur at twice the frequency of the SAW waves transduced by the device, eliminating the self cancellation for most practical cases [54].

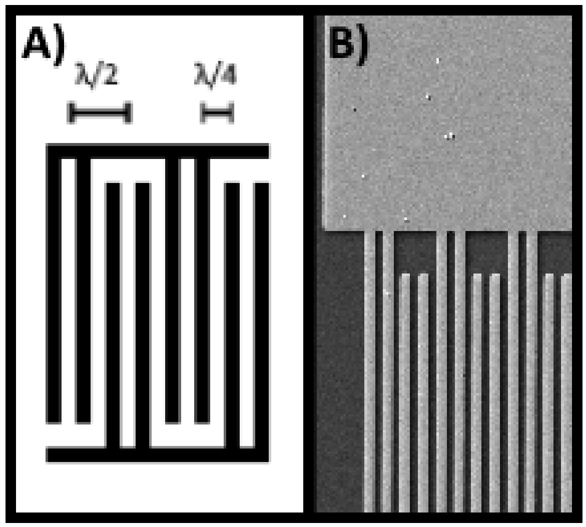

Figure 5: A) Annotated diagram of split transducer design for SAW devices noting key dimensions. As can be seen the periodicity of the IDT as an acoustic reflector is half that of it as a transducer; B) SEM image of fabricated device using split IDT SAW electrodes.

3.1.3 Impact of Thin Film Piezoelectric Thickness on Ideal SAW Operating Frequency

For SAW devices with transducer layers significantly thinner than the desired operating wavelength of the resonator, recent works have shown that the transduction efficiency is significantly impacted by the ratio of the film thickness h to the wavelength λ [55, 56]. Figure 6 presents results from recent works using finite element modeling showing a number of proposed operating curves for regimes wherein $h < \lambda$

As can be seen in Figure 6, there is a definite optimal ratio of h/λ for SAW devices where $h < \lambda$. Interestingly, the authors of these works proposes different, and mutually exclusive, ideal operating regimes. Thus in this work, device were produced that meet the suggested design requirements of each of these sources. This limits

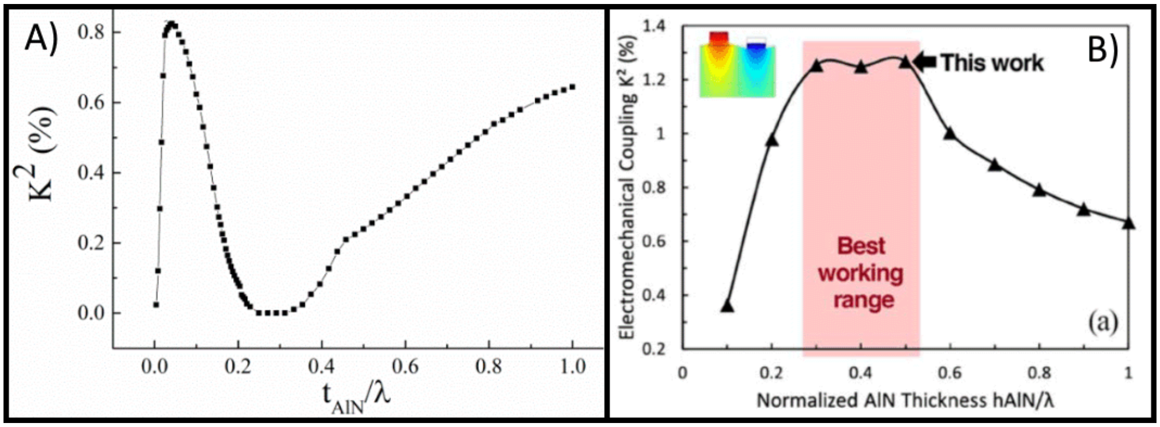

Figure 6: Plots of electromechanical coupling coefficient vs. transducer thickness from two sources for modeled AlN SAW resonators. A) [55]; B) [56]

the available operating frequencies to a narrow range where $0.05 < h/\lambda < 0.12$ and $0.28 < h/\lambda < 0.52$. For the 1 μm piezoelectric films used in this work, wavelengths were chosen to be 12 μm yielding a h/λ of 0.08 and 4 μm yielding a h/λ of 0.25. These values meet or are as close as possible to the required ratios of h/λ presented in the available research. For the thinner 200 nm samples of single crystalline scandium aluminum nitride ($Sc_{.3}Al_{.7}N$) used in this work, devices were limited to $h/\lambda = 0.05$ due to the limits of lithographic resolution available.

3.1.4 COMSOL Finite Element Analysis for SAW Devices

COMSOL Multiphysics was used to model the eigenfrequencies for both aluminum nitride (AlN) and 37% scandium aluminum nitride ($Sc_{.37}Al_{.63}N$) devices using the piezoelectric and solid mechanics toolboxes. Figure 7 shows the resulting mode shapes for a small section of the device surface (one wavelength) including all device layers for the AlN and $Sc_{.37}Al_{.63}N$ substrates respectively.

Using known material parameters in these models allowed for the estimation of the fundamental surface mode frequency. The results are presented in Table 2. The material parameters for the AlN, silicon, molybdenum and gold layers were assigned

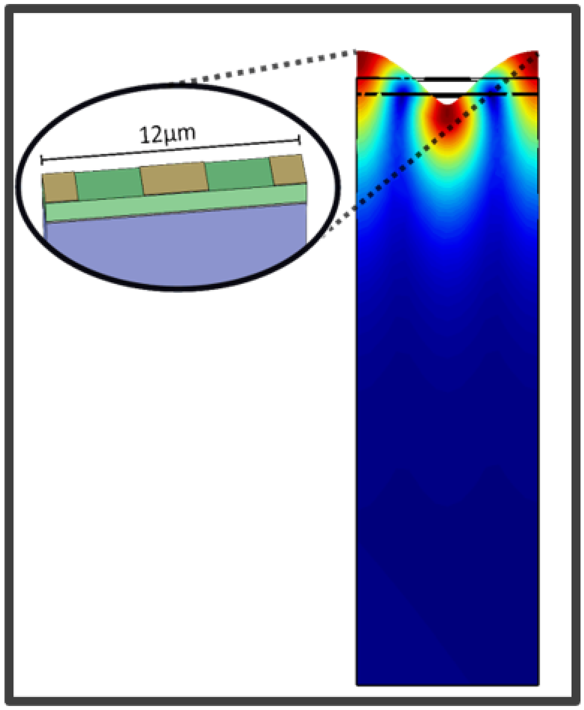

Figure 7: Finite element modeling of AlN and $Sc_{.37}Al_{.63}N$ SAW devices using COMSOL Multiphysics. Mode shapes are equivalent for AlN and $Sc_{.37}Al_{.63}N$, thus only one device is shown for brevity.

from the COMSOL default materials library. A custom material was defined for the $Sc_{.37}Al_{.63}N$ piezoelectric using information from recent works characterising the $Sc_XAl_{1-X}N$ films [11, 29, 30].

Table 2: Parameters used for finite element modeling of AlN and $Sc_{.37}Al_{.63}N$ SAW device and resulting fundamental surface wave frequency.

Parameter	**AlN**	**ScAlN**
Wavelength (μm)	12	12
Young's Modulus (GPa)	410	270
Shear Modulus (GPa)	129	80
Density (kg/m^3)	3300	3700
f_0 (MHz)	386	369

3.1.5 Length and Width Extensional Mode Design

Layouts for width extensional mode (WEM) devices operating directly at 23 MHz, 52.5 MHz, 115 MHz, 700 MHz were produced for the experimental phase of this work in order to cover a broad range of frequencies. Mechanically and electrically coupled filters were also produced using these resonators as building blocks. These low frequency resonators were also intended to serve as points of comparison for higher frequency overtone devices. The 700 MHz WEM resonator in particular provides a valuable point of comparison for the third overtone, 2100 MHz WEM resonator designs, as 700 MHz represents the fundamental mode of this resonator.

Also included were length extensional mode (LEM) devices operating at 23 MHz, 52.5 MHz, 115 MHz. LEM devices have been restricted to lower frequencies in this work due to lithographic and performance constraints on shrinking the physical dimensions of LEM resonators to achieve higher frequencies. The analysis of these devices was accomplished using analytical design tools and simulation.

The operating frequency of the LEM and WEM resonators is set by the device length and width respectively. And can be calculated as given by [12]:

$$f_0 = \frac{1}{2W}\sqrt{\frac{E_{eff}}{\rho_{eff}}} \tag{16}$$

for a WEM resonator. Where f_0 is the operating frequency of the resonator W is the width of the resonator, E_{eff} is the effective Young's Modulus of the entire device stack, and ρ_{eff} is the effective density of the device stack. This expression is equivalent for LEM resonators, requiring only that the length and width terms be swapped in (16). The size of the non-critical length or width dimension (for WEM and LEM resonators respectively) was set to be between 4-6 times the critical dimension to limit the propagation of lower frequency extensional modes to well below the frequency range of interest for the primary WEM or LEM mode. The equivalent

circuit parameters for the WEM resonators can be estimated analytically via the following equations [12]:

$$R_m = \frac{\sqrt{KM}}{Q\eta^2} = \frac{\pi}{4Q}\frac{\rho^{\frac{1}{2}}}{E^{\frac{3}{2}}}\frac{t}{L}\frac{1}{d_{31}^2} \tag{17}$$

$$C_m = \frac{\eta^2}{K} = \frac{4}{\pi^2}\frac{WL}{t}Ed_{31}^2 \tag{18}$$

$$L_m = \frac{M}{\eta^2} = \frac{\rho}{E}\frac{tW}{L}\frac{1}{4d_{31}^2} \tag{19}$$

Where Q is the Quality factor of the resonator, E is the Young's modulus of the resonator material, K is the stiffness of the resonator, η is the electromechanical coupling constant, ρ is the density, t is the thickness of the device, L is the length, and W is the width. These equations are again valid for LEM resonators also; requiring only that the length and width dimensions be swapped.

3.1.6 Overtone Width Extensional Mode Design

Third overtone width extensional resonators operating at 700 MHz, 1000 MHz, and 2100 MHz were designed using IDTs to excite the each frequency respectively. In a similar fashion to the fundamental mode resonators, the width of an N^{th} overtone WEM resonator can be calculated by:

$$f_0 = \frac{N}{2W}\sqrt{\frac{E_{eff}}{\rho_{eff}}} \tag{20}$$

Where the parameters are identical to those in (16) with the exception of the new parameter N which is the mode number of the overtone mode excited. The equation is equivalent for LEM resonators requiring only that the length and width terms be swapped in (20). The non-critical length or width dimension for the overtone

WEM resonators was set to be between 4-6 times the critical dimension to limit the propagation of lower frequency extensional modes to frequencies well below the frequency range of interest for the primary overtone WEM mode.

Overtone resonator equivalent circuit parameters can be calculated using (17), (18), and (19) in the same way that one would for resonators operating at the fundamental resonant frequency.

To transduce the overtone mode, IDTs are required with a pitch equal to $\lambda/2$. Figure 8 shows an image of the transducer electrodes for a third overtone WEM resonator designed to operate at 1000 MHz.

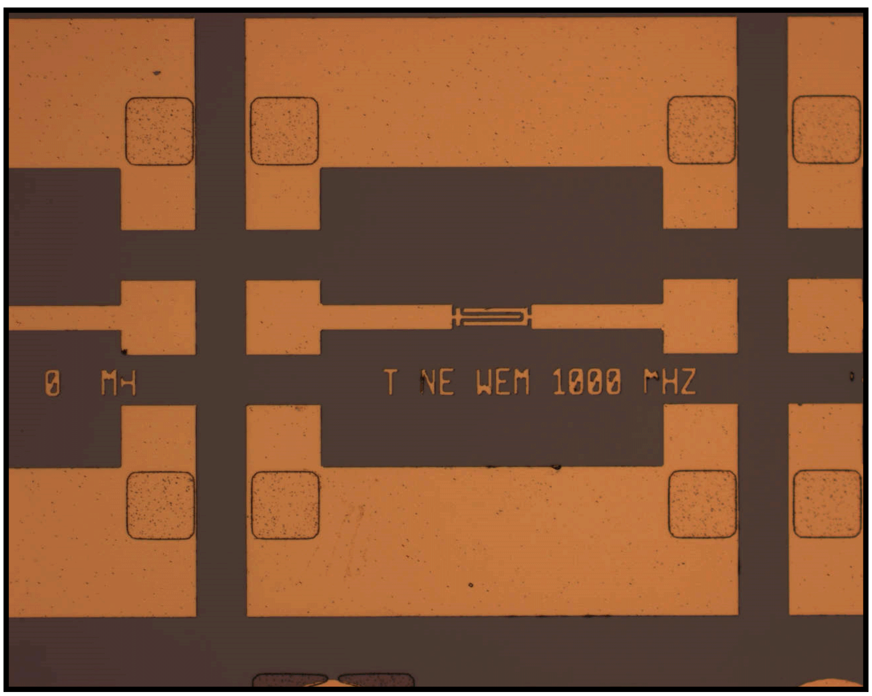

Figure 8: Example of metal IDT pattern for overtone WEM resonator.

3.1.7 Analytical Modeling for WEM and LEM Devices

For AlN and $Sc_{.37}Al_{.63}N$ transducer materials the the equivalent circuit parameters for the devices were predicted and these values are presented in Table 3. This modeling uses values for piezoelectric coefficients of $Sc_{.37}Al_{.63}N$ presented in previ-

ous works as the basis for predictions of device performance for a number of WEM resonators. The material properties assumed for the $Sc_{.37}Al_{.63}N$ film can be found at Table 4 [30, 57]. Equation (20) was used to calculate the width dimension for each resonator using the desired target frequency. The values for R_m, L_m, C_m were computed using (17), (18), and (19) respectively. The parasitic feed-through capacitance is given by C_0. C_0 is approximated by modeling the device electrodes as a parallel plate capacitor. Further discussion of these parameters can be found in Chapter IV.

Table 3: Analytical predictions for overtone $Sc_{.37}Al_{.63}N$ WEM resonators assuming a d_{31} value of 12 pm/V .

Harmonic	$\boldsymbol{Freq\ (MHz)}$	$\boldsymbol{R_m\ (\Omega)}$	$\boldsymbol{L_m\ (\mu H)}$	$\boldsymbol{C_m\ (fF)}$	$\boldsymbol{C_0\ (fF)}$	**Q**
1^{st}	700	48	9.8	28	0.78	500
3^{rd}	700	24	9.8	28	0.78	1000
1^{st}	1000	69	9.8	13	0.55	500
3^{rd}	1000	34	9.8	13	0.55	1000
1^{st}	2100	144	9.8	3	0.26	500
3^{rd}	2100	72	9.8	3	0.26	1000

Table 4: Material parameters assumed for $Sc_{.37}Al_{.63}N$ films from recent works [31, 39, 43]

Parameter	**value**
d_{31} (pm/V)	12
e_{31} (C/m^2)	2.5
E (GPa)	270
G (GPa)	80
ρ (kg/m_3)	3600

These predicted values reflect positively on the $Sc_XAl_{1-X}N$ piezoelectric as a transducer material, showing the potential for very high device performance. In particular the indicated motional impedance for a 2100 MHz overtone WEM resonator is excellent; approaching the hoped for value of 50 Ω and shows promise for operation at L-band frequencies. However, measured results will be required to confirm these values in practice.

3.2 Device Fabrication

3.2.1 SAW Device Fabrication

SAW resonators were produced using a simple one mask lift-off process to define the electrodes as shown at Figure 9. First a 2 μm coat of s1818 resist was applied to a clean substrate in accordance with Table 6. The mask was then direct written to the sample using the UV laser as discussed in Section 3.2.2 and developed. The chip with patterned resist was then ashed in O_2 plasma for 2 min at 200 W and 550 $mTorr$ to descum the pattern and ensure good adhesion of the metal layer. Molybdenum was sputtered over the pattern to a thickness of 50 nm in a Kurt J. Lesker Lab 18 sputter deposition system in accordance with the parameters listed in Table 5. Alternatively, some devices were evaporated with a 10 nm titanium as an adhesion layer and then 40 nm of gold. Lift off was conducted after metal deposition by placing the sample into a container of pure acetone and then placing the container in an ultrasonic bath for 5 min at room temperature. After removal from the bath the sample was cleaned and the devices tested.

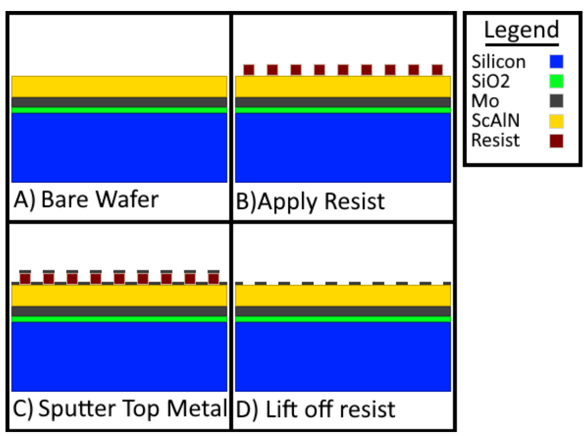

Figure 9: Annotated process flow for SAW device manufacture on $Sc_XAl_{1-X}N$ and AlN substrates. A) bare $Sc_XAl_{1-X}N$ wafer; B)Apply and pattern s1818 photoresist for lift off; C) Sputter top Metal; D) lift off resist and clean.

Table 5: Sputter deposition parameters used for molybdenum deposition in this work. Sputtering conducted in Kurt J. Lesker Lab 18 system.

Parameter	**Value**
Ignition Pressure (mTorr)	10
Rotation Speed (RPM)	5
Power (w)	200
Burn In (s)	10
Running Pressure (mTorr)	5
Deposition Rate (nm/min)	13.83

3.2.2 Direct Write to Chip for High Resolution Features

In order to reliably reproduce features at a scale of 1 μm it was necessary to direct write the masks to the test samples using the UV laser of a μPG 101 mask writer. Attempts to reproduce the needed features using a mask were unsuccessful utilising the available equipment. Attempts to reproduce features below 2 μm using the available MA/B6 mask aligner typically resulted in significant grating of the desired image, yielding unusable features. These issues were particularly notable for the SAW devices due to the large number of periodically spaced IDTs reflector gratings being prone to diffraction grating effects.

Masks were direct written to samples coated with 2 μm of s1818 photoresist prepared in accordance with Table 6. It should be noted that these settings were optimised for writing to the particular $Sc_{0.37}Al_{0.63}N$ and AlN films used in this work. Some variation in optimal parameters was noted between initial tests on silicon substrates and those on $Sc_{0.37}Al_{0.63}N$ and AlN. This likely results from differences in reflectivity and transmissivity of the substrate at UV wavelengths. As such, these settings may require modification for other substrate types.

Table 6: Preparation conditions used for high resolution direct write to s1818 photoresist

Thickness	**2 μm**
Spread Speed (rpm)	500
Spread Time (s)	5
Spin Speed (rpm)	4000
Spin Time (s)	60
Exposure Dose (mj/cm^2)	305
Developer	5:1 DI:351
Develop Time (s)	30

For the μPG 101 mask writer the optimal setting were found to be those presented at Table 7. It was also noted that the quality of the features reproduced by the mask writer were strongly dependant on the orientation of the features on the substrate. I.e. for continuous features such as the IDTs, the best results were achieved when these features were aligned with (parallel to) the path of the laser across the test chip. When these features were perpendicular to the path of the laser and small (near 1 μm) the features were significantly degraded as shown in Figure 10. It is believed that this degradation results from a inability of the mask writer laser to modulate itself at sufficient speed so as to be able to accurately reproduce these small features.

Table 7: Settings for direct write to 2 μm s1818 on $Sc_X Al_{1-X} N$ and AlN using μPG 101 mask writer.

Thickness	**2 μm**
Power (mW)	40
Duty Cycle	13%
Write Path	Uni-directional
Defocus	-2
Minimum resolution (μm)	0.75-1

3.2.3 AlN Device Fabrication

Unreleased AlN resonators were attempted in a 3 mask process with a final fourth mask proposed to defined etch windows for a backside potassium hydroxide (KOH)

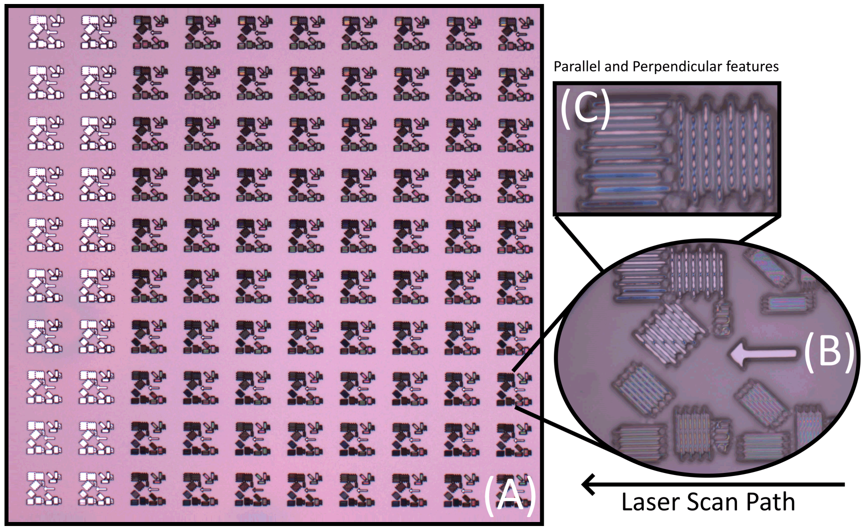

Figure 10: Test chip for direct write to s1818 for features parallel, perpendicular, and inclined to the laser path. A) direct write test layout; B) singular test pattern; C) close up of features parallel and perpendicular to the laser scan path.

etch release as required. The resonator bodies were defined using a 20% solution of KOH in de-ionised water to wet etch the AlN piezoelectric. The molybdenum electrode were defined with a CF_4 and O_2 plasma etch. Su-8 5 negative photoresist and s1818 positive photoresist were used for photolithography. Table 6 shows the spin and exposure parameters used in the application s1818 photoresist. Tables 17, and 18 show the processing conditions used for Su-8 5 resist.

The devices were produced on highly n-type doped {100} silicon wafer. A 100 nm layer of molybdenum was first deposited as the bottom device electrode. Disposition of 1 μm of AlN was then conducted as the transducer material via magnetron sputtering. This was the state in which the wafers were received from the external vendor.

Mask 1 was then applied to pattern 5 μm of Su-8 5 negative photoresist with a series of grounding vias through the piezoelectric material stopping at the bottom molybdenum layer. This etch was conducted using the 20% KOH etch described in Section 5.5.1. An additional 100 nm of molybdenum was then sputtered onto the top

of the piezoelectric layer making contact through the vias for the grounding electrode. This layer was also subsequently etched to define the device top electrodes. Sputtering parameters were as shown in Table 5. The second mask was then applied to define the top device electrodes. The top electrodes were etched via reactive ion etching (RIE) using the parameters in Table 8. The third mask then defined the resonator bodies and was used to first conduct a KOH etch through the AlN piezoelectric. A second etch using the same mask then breached the bottom electrode metal using CF_4 and O_2 plasma to etch the underlying molybdenum. Figure 11 shows an annotated diagram of the fabrication process used. Silicon nitride was deposited to a thickness of 300 nm onto the backsides of the samples as a hard mask for KOH etching of the silicon for releasing the AlN resonators.

Table 8: RIE settings for etching of molybdenum top metal

Parameter	**value**
CF_4 $(sccm)$	30
O_2 $(sccm)$	10
RIE (W)	75
ICP (W)	0
Pressure (mTorr)	50
Etch Rate (nm/min)	120

3.2.4 Polycrystaline ScAlN Device Fabrication

Attempts were made to fabricate released $Sc_{.37}Al_{.63}N$ devices in a 3 mask process with a vapor hydrofluoric acid (HF) release utilising a $\mu Etch$ vapour HF etcher. The devices were produced on an highly n-type doped {100} silicon wafer. A 500 nm layer of SiO_2 was deposited onto the wafer to allow for later HF release of the devices. Molybdenum was then sputtered to a thickness of 100 nm to form the bottom device electrode. Next the transducer layer was deposited as 1 μm of highly textured $Sc_{0.37}Al_{0.63}N$ via magnetron sputtering. X-Ray diffraction (XRD) data provided by

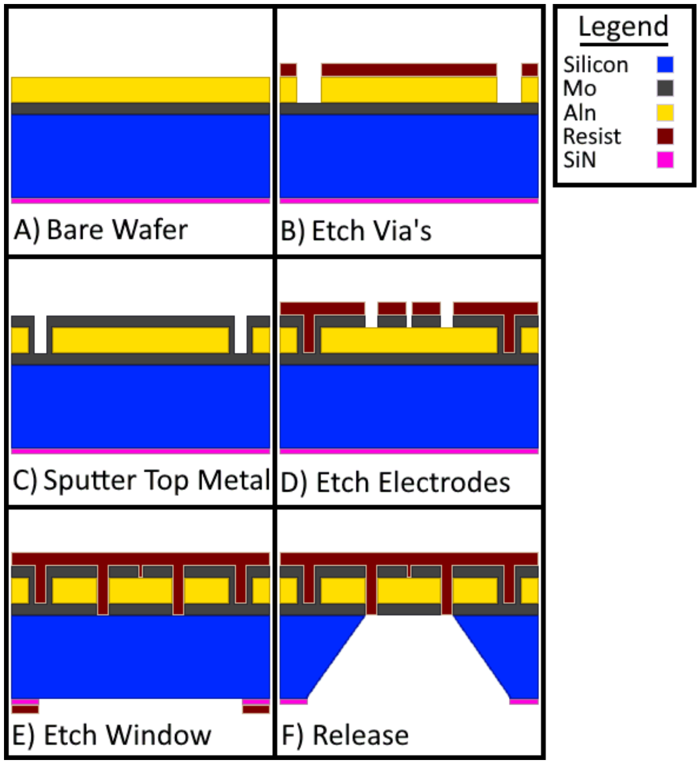

Figure 11: Annotated process flow for AlN device manufacture. A) wafer received from external foundry prior to processing; B) apply Su-8 photo mask and KOH etch via's to bottom metal; C) strip resist and sputter top metal; D) apply s1818 resist and pattern top electrodes; E) strip resist and apply thick 5 μm Su-8 to top side, apply s1818 to bottom side and pattern SiN etch windows for KOH back side release; F) Strip s1818 only and immerse in KOH for etch release.

the foundry (OEM Group) indicates an excellent rocking curve value of $1.8 - 1.9°$ for the film. The wafers used in this work were received from the foundry in this condition.

Mask 1 was then used to pattern a series of grounding vias through the piezoelectric material stopping at the bottom molybdenum layer.

These vias were etched through RIE with BCl_3 and Cl_2 plasma. Molybdenum was then sputtered to a thickness of 100 nm over the top of the piezoelectric layer making contact through the vias and providing the device top metal. The second mask was then applied to define the top device electrodes through RIE of the top

metal. The third and final mask then defines the resonator bodies and is used to conduct two separate RIE steps. The first etches through the piezoelectric layer to define the resonator bodies using the same BCl_3 and Cl_2 plasma used in step one. The second etch breaches the bottom electrode metal using CF_4 and O_2 plasma to etch the molybdenum bottom metal layer. Finally the devices were released using a vapor HF release. Figure 12 shows an annotated diagram of the manufacturing process used. However, issues with the etching of the $Sc_{.37}Al_{.63}N$ material were experienced and will be further discussed in Section 5.5.0.1.

3.2.4.1 Single crystalline ScAlN Device Manufacture

Single crystalline specimens of $Sc_{30}Al_{70}N$ were provided by Air Force Research Laboratory (AFRL). Specimens were 200 nm $Sc_{30}Al_{70}N$ deposited on 100 nm titanium nitride (TiN) on a Al_2O_3 substrate. These specimens were used to prepare SAW devices as described in Section 3.1.2.

3.2.5 Masking for KOH Wet Etches

For the KOH wet etching processes investigated in this work several materials were investigated as possible masks for both the top side and bottom side of the devices. The need for both suitable and practical top and bottom side masks was necessitated by the AlN devices developed in this work requiring a backside etch release. In particular the backside etch release requires a very robust masking of the silicon due to the long etch times required to etch 550 μm of silicon from the wafer backside.

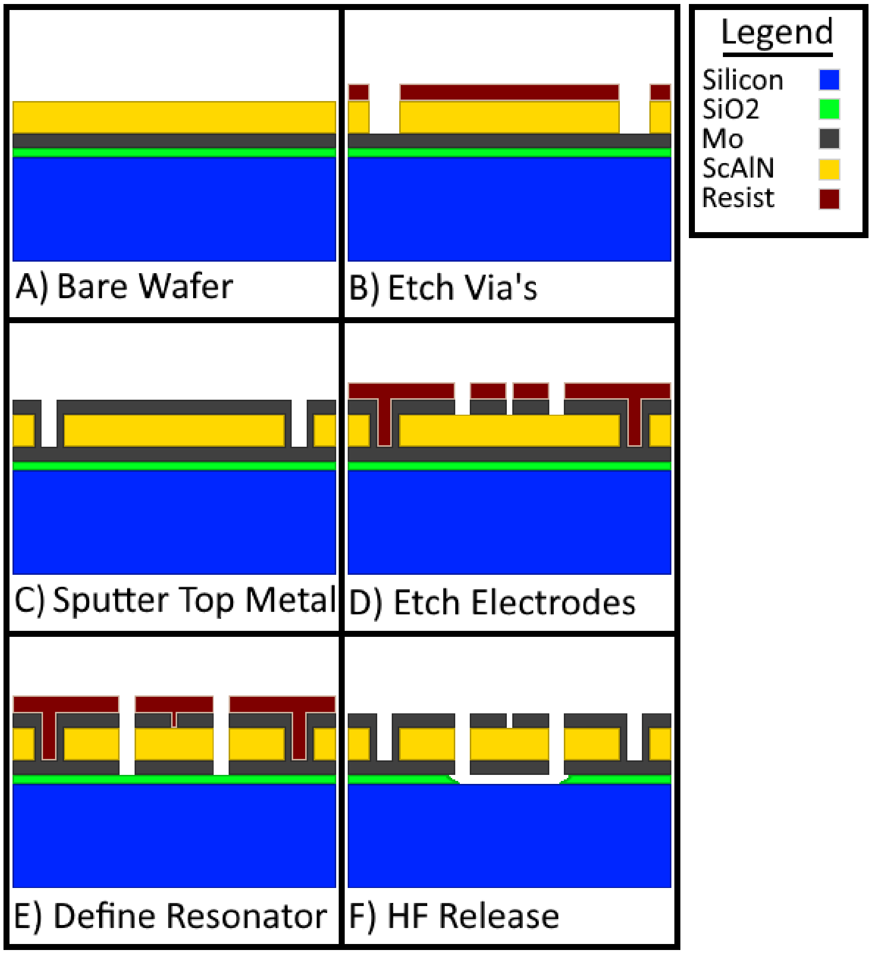

Figure 12: Annotated process flow for poly $Sc_{.37}Al_{.63}N$ device manufacture. a) bare wafer prior to processing as received from foundry; b) Su-8 photo mask applied and via's etched to bottom meta; c) photo mask stripped and top metal sputtered; d) s1818 resist applied and top metal electrodes patterned; e) s1818 stripped and Su-8 mask applied, RIE etch of $Sc_{.37}Al_{.63}N$ and RIE etch of bottom metal (different chemistries); f) HF release of resonator body.

3.2.5.1 Nickel Hard Mask

Hard masks were investigated using nickel due to it's availability, high chemical resistance and it's common use as a hard mask in many dry etching processes. $100-250$ nm films of nickel were sputtered onto silicon $\{100\}$ substrates for testing in KOH solutions. Test etches were conducted in 20% w/w KOH solution in DI water at $60°C$. However, results for a nickel hard mask in KOH were objectively very poor,

with mask separation occurring in a matter of minutes with some samples lasting as long as 10 minutes. This was far less than the 5-10hr needed to etch the full depth of the silicon wafer.

Table 9: Sputter deposition parameters used for nickel deposition in this work. Sputtering conducted in Kurt J. Lesker lab 18 system.

Parameter	**Value**
Ignition Pressure (mTorr)	10
Rotation Speed (RPM)	5
Power (w)	200
Burn In (s)	10
Running Pressure (mTorr)	5
Deposition Rate (nm/min)	9

It is believed that excessive micro-porosity in the deposited nickel film was root cause of the rapid loss of the nickel hard mask. This porosity would allow the KOH solution to penetrate the mask and directly attack the underpinning silicon [58]. The nickel films were deposited using a Kurt J. Lesker Lab 18 sputter deposition system under the conditions listed in Table 9. Direct measurement of the porosity of the nickel film was not possible with the equipment available. However, a qualitative analysis of the nickel hard mask surface was conducted using scanning electron microscopy. Figure 18 shows two representative images from this analysis. From these images it can be qualitatively observed that the nickle hard mask shows high porosity with numerous voids visible in the material surface. Thus it was concluded that high porosity was likely contributory to the failure of the nickel hard mask material. As the hard masking was simply a means to an end and not a core focus of this work an alternative hard mask using SiN was successfully employed. However, this necessitated the involvement of an external collaborator at AFRL.

These results indicate that sputtered nickel is likely an unsuitable material for wet etch hard masking under the deposition conditions listed. It may be possible to use this material as a hard mask with further refinement to the deposition process.

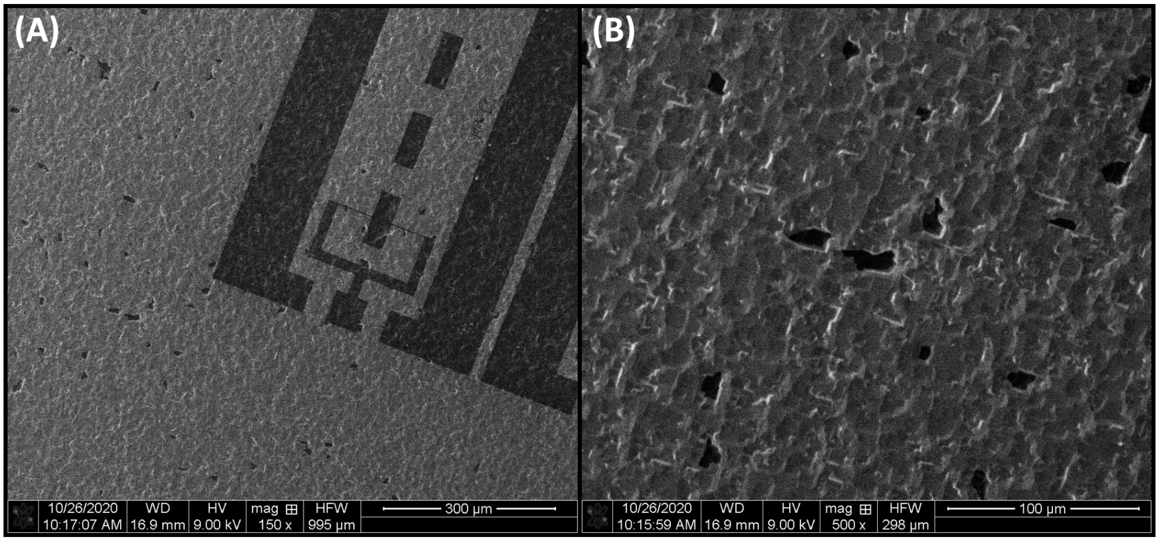

Figure 13: SEM imagery showing the nickel hard mask with test pattern at high magnification deposited directly onto a silicon 100 substrate via sputtering. Surface porosity is clearly visible.

3.2.5.2 Su-8 Mask

Su-8 negative photoresist was used to mask the top side of chips both for etching of the resonator structures and as a protective coating during the backside etch release of AlN devices in KOH. This work was inspired by a paper title *Improved adhesion in hybrid Si-polymer microelectromechanical systems (MEMS) via micro mechanical interlocking* by M P Larsson, R R A Syms and A G Wojcik [59]. In this work the authors propose the use of interlocking micromechanical structures on the surface of a chip in order to maximise the adhesion of polymer coatings to the substrate. The authors then demonstrate a full depth KOH etch using the presented techniques.

In order to protect the device side of the chips during the KOH backside release a hybrid approach was used wherein both the resonator bodies themselves and inter-

locking pits were used to maximise adhesion to the substrate. Furthermore care was taken during Su-8 coating to ensure that the Su-8 film also covered the edges of the chips to prevent lifting of the film [59]. This was achieved via flooding the substrate with SU-8 prior to spinning and allowing the photoresist to flow over the edges of the chip. Slow spin speeds were also used to maximise film thickness and prevent loss of the edge coating. The spin and exposure parameters used during this process are presented in Tables 17 and 18.

IV. Testing Methodology

4.1 Parameter Extraction

The Butterworth Van-Dyke (BVD) mechanical resonator model was used to extract the equivalent circuit parameters from the piezoelectric resonators. Figure 14 shows the equivalent circuit model for a BVD mechanical resonator. The transfer function of the equivalent circuit can be expressed as:

$$Z_{BVD} = \frac{1}{sC_0} \frac{s^2 L_m C_m + sR_m C_m + 1}{s^2 L_m C_m + sR_m C_m + 1 + \frac{C_m}{C_0}} \tag{21}$$

From the transfer function, the following relationships can be made between the measurable resonator frequency response and the electrical equivalent parameters:

$$\omega_s = \sqrt{\frac{1}{L_m C_m}} \tag{22}$$

$$\omega_p = \omega_s \sqrt{1 + \frac{C_m}{C_0}} \tag{23}$$

$$Q = \frac{1}{\omega_s R_m C_m} = \frac{\omega_s L_m}{R_m} \tag{24}$$

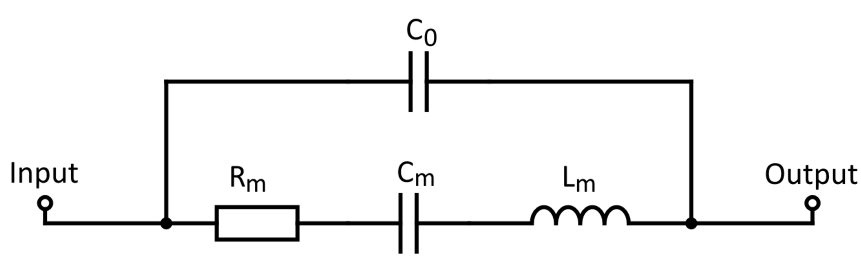

Figure 14: Two port mechanical resonator BVD electrical equivalent circuit.

Where ω_s is the series resonant frequency of the measured device, ω_p is the parallel resonant frequency, L_m and C_m are the motional inductance and capacitance of the resonator respectively, R_m is the motional resistance of the resonator, and C_0 is the parasitic feed through capacitance. Each of these parameters can be estimated from the frequency response of an individual device and processed using a simple automated script to produce the equivalent circuit parameters. An annotated frequency response curve illustrating the measurement of each of the required parameters is at Figure 15.

A typical process flow would be to measure Q directly from the frequency response of the device by measurement of the series resonant frequency and the $-3\ dB$ bandwidth of the series resonance as given by:

$$Q = \frac{f_0}{\Delta f} \tag{25}$$

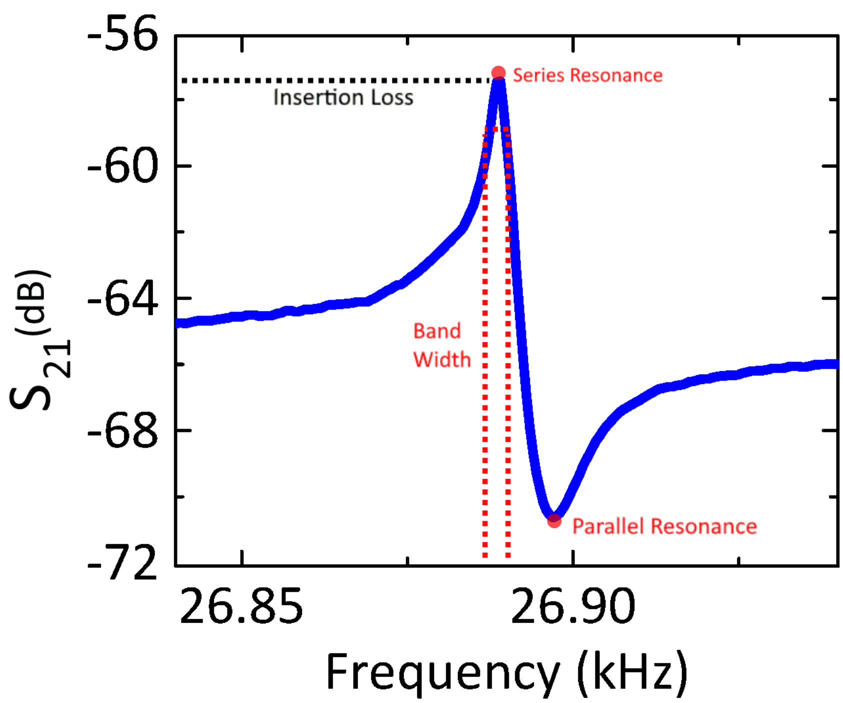

Figure 15: Example frequency response curve for a mechanical resonator, annotated for BVD electrical equivalent circuit parameter extraction

The series and parallel resonant peaks can be directly measured from the S_{12} or S_{21} parameters. The s-parameter measurement can then be converted to impedance parameters (Z-parameter); where-in the impedance of the Z-parameter at series resonance will correspond to the motional resistance of the resonator as the impedance of a mechanical resonator is approximately real at resonance. Using these known values (24) can be rearranged to solve for L_m

$$L_m = \frac{QR_m}{\omega_s} \tag{26}$$

Equation (22) can then be rearranged to solve for the motional capacitance C_m

$$C_m = \frac{1}{\omega_s R_m Q} \tag{27}$$

Finally (23) can be rearranged to solve for the parasitic feed-through capacitance C_0.

$$C_0 = \frac{C_m}{(\frac{\omega_p}{\omega_s})^2 - 1} \tag{28}$$

4.2 Mechanical Testing

Mechanical testing of the resonators and filters exposed them to a variety of vibrations in order to assess the robustness of the devices to environmental factors. Of particular relevance to this work are the shocks and vibrations typical of launch and space environments.

Vibrational loads were simulated using a Mini-shaker Type 4810 from Brüel & Kjær. Test samples were wired bonded into a dual inline package (DIP) and fitted to a custom breakout PCB. This PCB could then be fitted to the actuator of the Mini-shaker and a variety of vibrational frequencies tested. The Mini-shaker was

driven via an arbitrary waveform generator buffered by a KROHN-HITE Model 7500 Wideband Amplifier. Scattering parameters where measured on an Agilent 5222a network analyser. A diagram of the test configuration is provided at Figure 16. Please note that this testing methodology only monitored the vibrational frequency. The vibrational amplitude and acceleration was not measured during testing due to limitations of the setup.

This allowed for a variety of realistic vibrations to be tested based on vibrational frequencies likely to be experienced during space launch and whilst in orbit. Representative frequencies of interest were determined from several relevant sources [36,37,60]. These works indicated that vibrational frequencies in the range of $0 - 2000\ Hz$ are most severe in launch and space environments; with vibrations being particularly harsh under $1000\ Hz$.

The frequency responses of the packaged device was then measured whilst under external vibrational loading to determine the impact to device performance. Vibra-

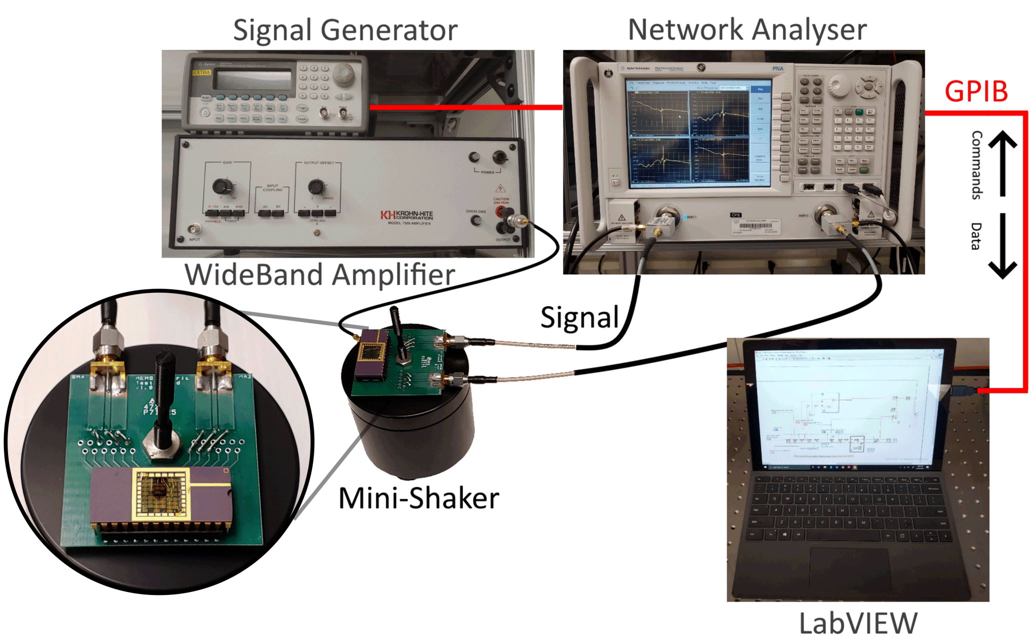

Figure 16: Diagram of test equipment configuration for vibrational testing of resonators. Including GPIB connections, signal, and mini shaker driver.

tional frequencies between $0 - 2000$ Hz were tested at intervals of 10 Hz with the resonant frequency of the S12 parameter sampled five times consecutively at each point to provide an average value. The data was captured at a frequency resolution of 250 Hz to ensure that small variations in the resonant frequency were captured. The standard deviation of the measurements could also be computed as a measure of the uncertainty present in the data. Data collection was automated using LabVIEW software over a GPIB connection to control the signal generator and automate data capture on the network analyser.

The general procedure for testing was as follows. First the network analyser (NA) was configured for the sweep, power, and trigger settings required. Limitations of the test set-up prevented typical SOLT calibration. However, this was determined to not be a significant factor in vibrational testing as the center frequency measurement of the resonator will not be affected by the un-calibrated measurement so long as parasitic effects are negligible. The NA was then connected to the test board with a single chosen device wire-bonded to the test terminals. The test PCB could then be mounted to the shaker by means of a single central mounting nut. The signal generator and NA were connected together via GPIB and then jointly connected to a computer via a GPIB to USB converter for automated data acquisition and instrument control. A LabVIEW virtual interface then cycled the signal generator through the full range of vibrational frequencies and automated the capture of data from the NA at each step. The frequency response data was then exported to MATLAB for processing of the resulting data sets. From this data the relative deviation of the excited response from the resting response could be determined.

4.3 DC Frequency Tuning

DC frequency tuning was conducted using bias-T fittings and a DC power supply to simultaneously allow for connection to a DC source and network analyser for measurement. Each probe and the probe station chuck were connected to a common ground to ensure a common reference level. The DC bias was then stepped from $-25\ VDC$ to $25\ VDC$ in steps of $5\ VDC$. At each point 5 measurements were taken in order to allow for the averaging out of any jitter from the measurements. The probe station was also vibrationally isolated and measurements were taken with care not to disturb the test set-up. A frequency range of $10\ MHz$ was set centered on the resonant peak of the resonator with 32001 points sampled yielding a frequency resolution of $312\ Hz$ to ensure that small variations in frequency could be captured. Figure 17 shows a diagram of the testing configuration.

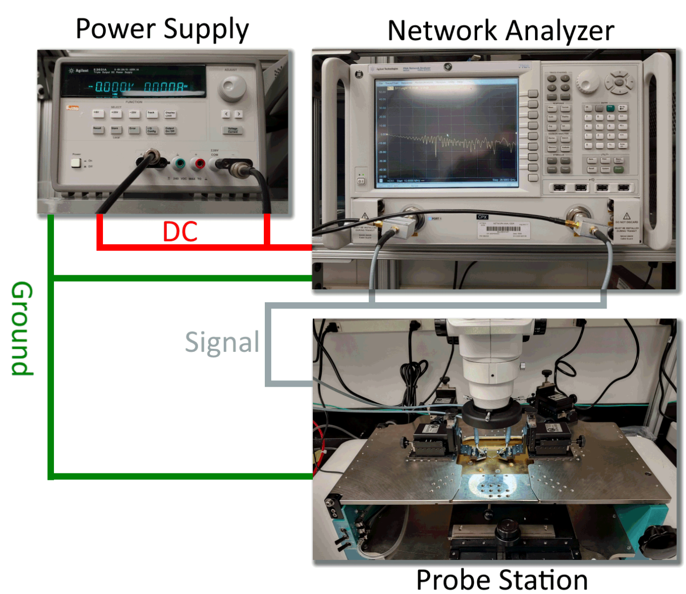

Figure 17: Test configuration used in this work to measure the effects of DC biasing on the center frequency of resonators. DC biasing is provide through the use of bias-T attachments at network analyser ports. A common ground reference is provided by the DC power supply.

4.4 Estimation of RF Losses for Titanium Nitride and Molybdenum Top Metal

The magnitude of the RF losses posed purely by the top metal electrodes of the devices was estimated through the measurement of the transmission s-parameters for shorted top metal electrodes. This accounts for a range of interactions causing loss, including resistance and capacitance. Figure 18 shows an example of a representative shorted device.

The transmission s-parameters S_{12} and S_{21} then indicate the approximate magnitude of the RF losses across the range frequencies tested for the top metal only. From these results estimates of the RF losses can be made and general conclusions regarding the suitability of the material as an RF electrode for MEMS devices. These results will also be supported through measurements of the sheet resistance of the metal film. Sheet resistance measurements were made in $\Omega/\Box$ using a Jandel Model RM3-AR four point probe calibrated against an indium tin oxide reference standard.

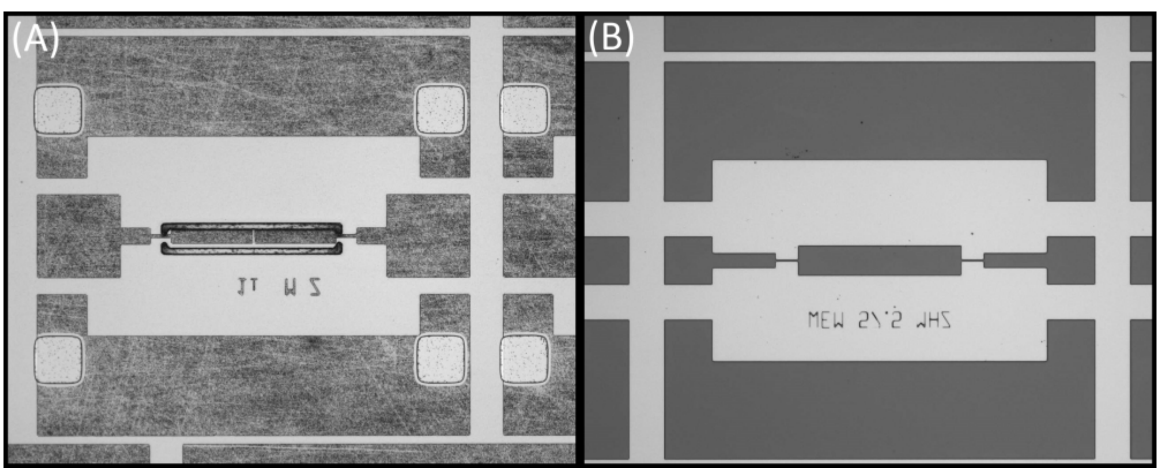

Figure 18: Exampled of shorted resonator top metal electrode to allow the magnitude of the RF losses to be quantified. A) Unreleased resonator with normal electrode; B) RF loss test pattern, with shorted TiN electrodes

4.5 Calculation of Electromechanical Coupling Coefficient for SAW Devices

The electromechanical coupling coefficient κ^2 for a surface acoustic wave (SAW) resonator can be given by the relationship between the phase velocity of the metallized device ν_m and the free surface (unmetallized) phase velocity ν_0 [55]:

$$\kappa^2 = 2 \times \frac{\nu_0 - \nu_m}{\nu_0} \tag{29}$$

The measured center frequency of a SAW resonator f_0 and the device pitch P can be used to directly solve for ν_m by re-arranging (9). However, in the first instance the variable ν_0 is not known for the substrate. To determine ν_0, the electromechanical coupling coefficient can first be determined by the relationship of the series and parallel resonance for a 2-port resonator [61]:

$$\kappa^2 = \frac{\pi}{2}\frac{f_s}{f_p}tan\left[\frac{\pi}{2}\left(\frac{f_p - f_s}{f_p}\right)\right] \tag{30}$$

So long as the measured 2-port device is constructed on an identical substrate and any devices are relatively far apart, such that the metallization of other nearby devices does not impact the response of the tested device, (29) can be rearranged to solve for ν_0 as:

$$\nu_0 = \frac{-\nu_m}{\left[\frac{\kappa^2}{2} - 1\right]} \tag{31}$$

Whilst (30) can be used to determine κ^2 for 2-port devices, solving for ν_0 allows for the calculation of κ^2 using (29). This is a more general form that can also be applied to 1-port devices. Equation (30) cannot be used to solve for the κ^2 values of one port devices as they do not display a parallel resonance.

V. Results and Analysis

5.1 Preamble

Due to difficulties in the fabrication of width extensional mode (WEM) and length extensional mode (LEM) devices in this work, only surface acoustic wave (SAW) resonators were available for testing. Furthermore, through the testing conducted in this work, molybdenum and titanium nitride (TiN) proved unsuitable for use as top metal electrodes without further refinement of the deposition process. As such the results in this section reflect only devices with gold electrodes. Due to issues with equipment, analysis of temperature effects could not be conducted.

5.2 Titanium Nitride and Molybdenum Top Metal RF Losses

The radio frequency (RF) scattering parameters S_{12} and S_{21} were measured for a variety of shorted electrode topologies. The average transmission losses for these devices are presented in Table 10 and can be used to estimate the magnitude of RF losses induced by the top metal. Also presented are measurement of the sheet resistance for the metal films deposited in this work.

Table 10: Average S_{12} RF losses for molybdenum and TiN top metal electrodes. RF losses are measured from 10-8000 MHz.

Material	**Moly 200 nm on Si**	**Moly 50 nm on ScAlN**	**TiN 104 nm on Si**
Average RF Loss (dB)	-	-50	-37
Sheet Resistance ($\Omega/\square$)	.07836	530.77	25.29

From these results it can be qualitatively concluded that use of TiN as an electrode material will likely result in high RF losses. TiN electrodes show both significant RF losses from 10 MHz to 8 GHz in addition to significantly higher sheet resistance when compared to thicker (200 nm) molybdenum films.

At the time of publishing, no supporting evidence for TiN films of lower resistivity than those measured in this work could be found. Given that molybdenum has a melting point of $2623°C$ vs. $2930°C$ for TiN, there is no significant benefit to the use of TiN as a high temperature electrode material. However, whilst research shows that low sheet resistance can be achieved with molybdenum films under the correct processing conditions, the very thin (50 nm) films of molybdenum deposited on 37% scandium aluminum nitride ($Sc_{.37}Al_{.63}N$) in this work showed unacceptably high sheet resistance and average RF losses.

To further verify these results, SAW devices using proven layouts were produced utilizing 50 nm molybdenum films deposited with same techniques as those used for sheet resistance test samples. As predicted however, no discernible resonances could be detected from these devices due to high RF losses.

This prevented the use of molybdenum as a top metal in this work. Further study will need to be conducted to determine whether thin films of molybdenum can be deposited at an acceptable quality in house on scandium aluminum nitride ($Sc_XAl_{1-X}N$). Otherwise, future works may need to engage external vendors or collaborators for deposition. The experience gained in this work does however indicate that high quality films of both aluminum nitride (AlN) and $Sc_XAl_{1-X}N$ can be grown on molybdenum films. With the $Sc_XAl_{1-X}N$ films delivered from external vendors achieving Rocking Curve values of $1.8 - 1.9°$. As such, molybdenum remains a promising candidate for a high temperature electrode material.

5.3 Electrical Characterisation of SAW Devices

5.3.1 Polycrystalline Scandium Aluminum Nitride Devices

The $Sc_{.37}Al_{.63}N$ SAW devices produced in this work displayed moderate Q factor in vacuum and low insertion losses. Figure 19 shows the measured $S12$ transmission

for a 369 MHz SAW resonator. All resonator electrical measurements were conducted in a vacuum of 2×10^{-6} $Torr$.

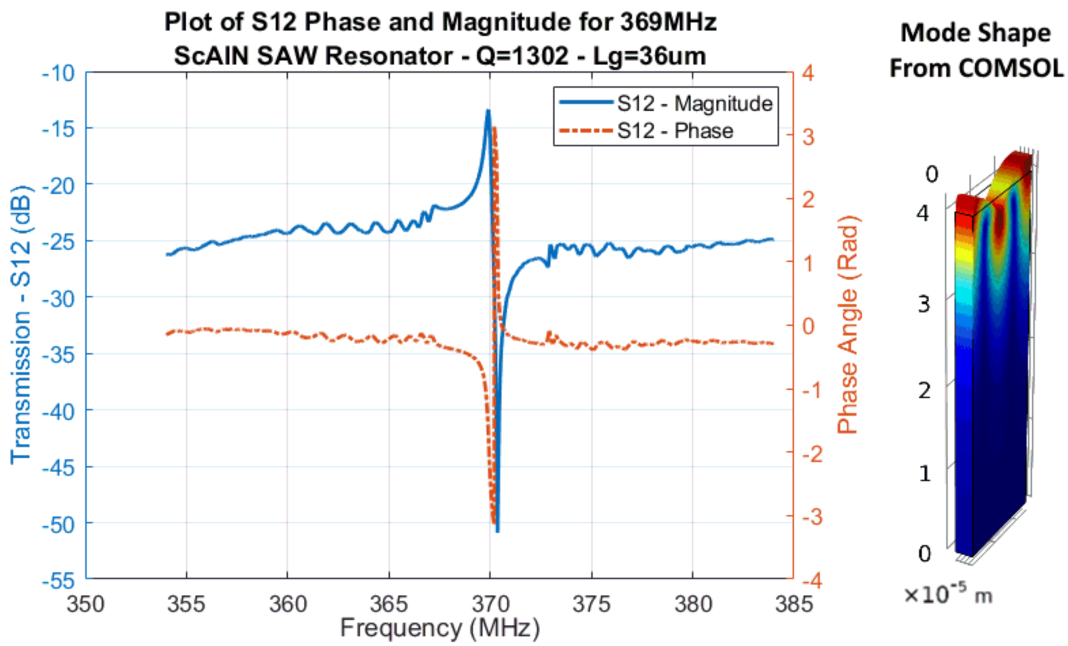

Figure 19: S12 magnitude and phase for 369 MHz $Sc_{.37}Al_{.63}N$ SAW resonator using split electrode design.

Results for each of the tested devices, including Butterworth Van-Dyke (BVD) parameter extraction are presented in Table 11

Table 11: Electrical characteristics including Butterworth Van-Dyke equivalent circuit parameters for 2 port split transducer polycrystalline $Sc_{.37}Al_{.63}N$ SAW devices.

f_0 (MHz)	R_m (Ω)	L_m (μH)	C_m (fF)	C_0 (pF)	Q	N_r	L_g (μm)	κ^2
394	43.94	16.88	10.87	4.13	897	400	12	0.32%
370	45.74	17.98	10.26	2.85	919	100	36	0.44%
369	40.64	22.77	8.13	3.28	1302	200	36	0.31%
370	40.74	14.81	12.41	4.54	848	100	36	0.34%
396	43.95	7.94	23.09	5.26	422	400	72	0.54%
370	40.33	30.98	5.88	–	1800	100	164	0.35%

These results reflect positively on the $Sc_{.37}Al_{.63}N$ material showing motional impedance values below the desirable threshold of 50 Ω. From these results the

effective acoustic velocity of the the $Sc_{.37}Al_{.63}N$ substrate with gold electrodes can be determined using (33). Thus for the $Sc_{.37}Al_{.63}N$ substrate used in this work the acoustic velocity can be calculated as $\nu_{ScAlN} = 4440\ m/s$.

These results also confirm theoretical predictions regarding the relationship between the effective cavity length of the acoustic cavity $L_{c_{eff}}$ and the Q factor of the resonator. Here Q can be seen to rise with increasing L_g, between the input and output interdigital transducers (IDTs) due to the larger acoustic cavity. However, extremely large cavities show some reduction in Q, likely due to leakage from diffraction of the acoustic energy out of the cavity over the larger distance $L_{c_{eff}}$. Other losses also rise with increasing cavity length as discussed in Section 3.1.2 of this work. Increasing the acoustic aperture of the devices could mitigate these effects somewhat as this will reduce diffraction of the SAW energy out of the cavity. This will not mitigate other losses however.

Also observable is a significant increase in the Q of the resonators with increasing number of reflectors. For the reflectors produce in this work no major increases in Q were notable past $200 - 400$ reflectors. This confirms the estimation of the grating reflectivity made in Section 3.1.2 of this work by implying that unity reflectivity is reached with less than 200 reflector gratings.

The electromechanical coupling achieved by these devices also compares favorably with the maximum theoretical values achievable for thin films as presented in Figure 6 and the source work [55]. Whilst the theoretical results predict a maximum κ^2 value of approximately 0.8% for thin film SAW devices, in practice their work achieved a maximum value of $\kappa^2 = 0.57\%$.

Figure 20 shows scanning electron microscope (SEM) imagery of the completed 12 μm wavelength split IDT SAW resonators.

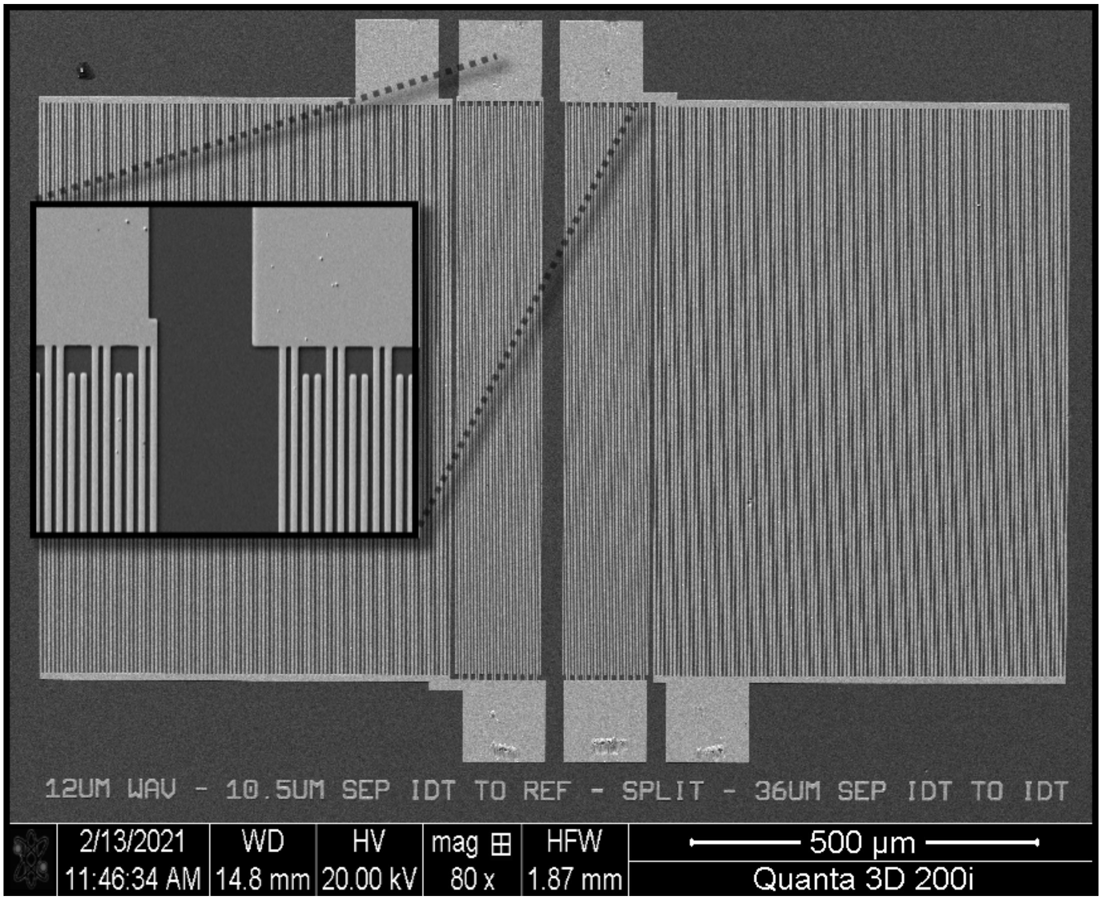

Figure 20: SEM image of split IDT device with 12 μm wavelength. Inset image shows close up of split finger IDTs.

5.3.2 Frequency Tunability of Polycrystalline Scandium Aluminum Nitride Devices

The $Sc_{.37}Al_{.63}N$ SAW devices did not show appreciable frequency tunability in response to a DC bias voltage. Figure 21 shows a plot of the measured center frequency for a 370 MHz SAW resonator in response to a DC bias from -25 *to* $25V$. This figure shows no clear trend in the center frequency of the resonator in response to the DC bias voltage. At each DC bias voltage, the standard deviation of the series resonant frequency is approximately 5 kHz. This indicates that what little variation can be observed is likely noise in the measurement. However, the SAW devices are an

non-ideal case for this technique due to the lack of a suitable grounding plane in the device stack. This necessitated the use of the probe station chuck as the grounding plane. Resonator architectures such as WEM or LEM may see more significant tuning ability due to the far smaller gap between the electrodes and grounding plane.

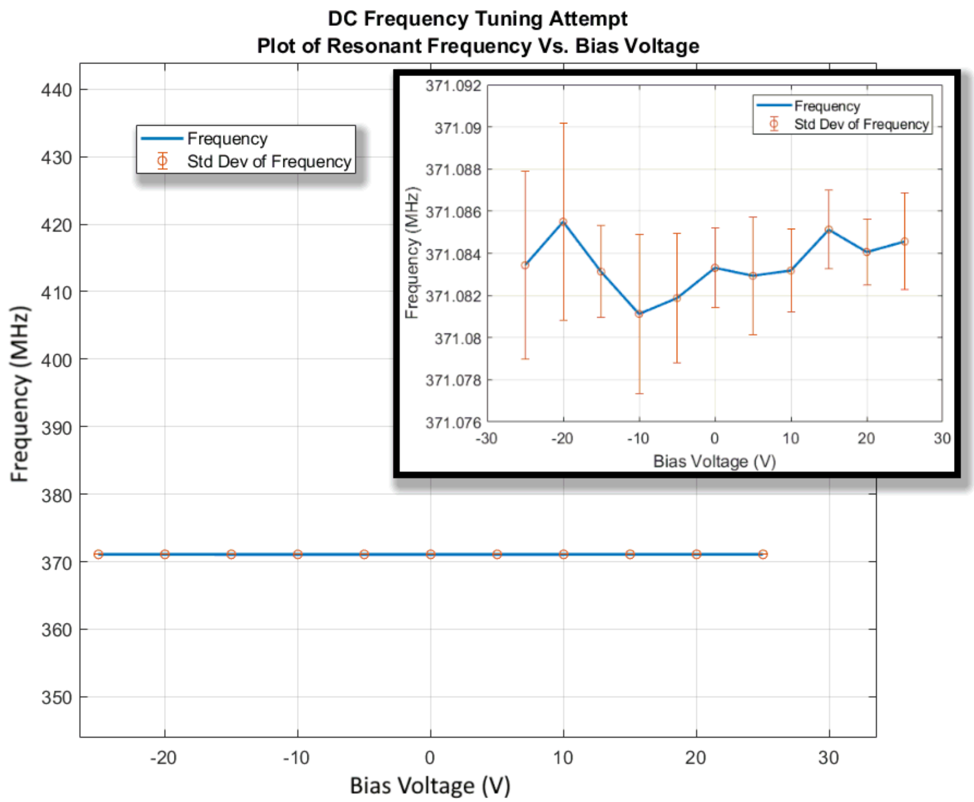

Figure 21: Plot of SAW resonator center frequency vs. DC bias voltage across substrate for 370 MHz $Sc_{.37}Al_{.63}N$ SAW device.

The effective electric field strength can be calculated as:

$$E_{bias} = \frac{V_{bias}}{D} \left(\frac{V}{m}\right) \tag{32}$$

Where V is the bias voltage applied and D is the distance to the ground plane. For the purpose of this testing, the ground plane is the highly n-type doped silicon substrate. For the sample tested $D \approx 1.6\ \mu m$, accounting for the thickness of the piezoelectric layer, the underlying molybdenum, and the silicon dioxide layer. Thus

the electric field strength is $15.62MV/m$. This is a significant field strength, and demonstrates that the SAW devices produced in this work are highly resistant to the effects of external electric fields.

5.3.3 Single Crystal Scandium Aluminum Nitride Devices

SAW devices predicted to operate at 1.1 GHz were fabricated on a test sample of scandium aluminum nitride ($Sc_{.3}Al_{.7}N$). Figure 22 shows such a device. However, no detectable resonances could be found. It is believed that these devices were impacted by the very thin film available for testing and limitations of the lithographic tools available. These films were only $200nm$ thick and as such even with $1\mu m$ resolution the ratio h/λ was 0.05. This is below the ideal threshold predicted in other works as discussed in Section 3.1.3, thus the feasibility of these devices was uncertain. Furthermore, the single crystal thin films provided were still in a developmental stage, thus the film quality could have impacted these results.

5.3.4 Aluminum Nitride Devices

Several AlN SAW devices were produced in this work showing high Q factor in vacuum and moderate insertion losses. Figure 23 shows the measured $S12$ parameter for a 395 MHz AlN SAW resonator. All resonator electrical measurements were conducted in a vacuum of 2×10^{-6} $Torr$. Results for each of the devices including BVD parameter extraction are presented in Table 12

Table 12: Electrical characteristics including Butterworth Van-Dyke equivalent circuit parameters for 2 port split transducer AlN SAW devices.

f_0 (MHz)	R_m (Ω)	L_m (μH)	C_m (fF)	C_0 (pF)	Q	N_r	L_g (μm)	κ^2
394	78.85	37.71	4.33	3.35	1184	400	12	0.16%
395	78.05	69.38	2.34	1.54	2207	100	36	0.19%
397	75.41	75.3	2.14	2.07	2489	400	72	0.13%
396	79.76	51.1	3.16	–	1594	100	164	0.24%

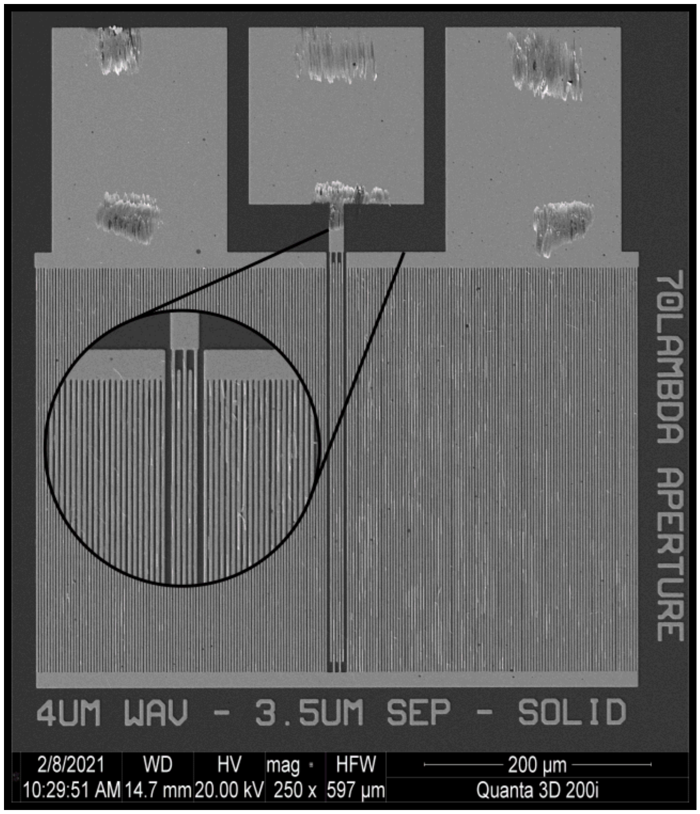

Figure 22: SEM image of 4 μm wavelength resonator on single crystal $Sc_{.3}Al_{.7}N$ substrate. Markings on pads are from probe tip contact.

The Q values achieved indicate a very high quality AlN film. The highest performing AlN resonators in this work achieve a figure of merit (FOM) of 9.83×10^{11}. This is quite a respectable value within less than two orders of magnitude of the predicted Akhiezer limit for AlN [5].

Overall insertion loss of the AlN resonators remains somewhat high for applications as front end components. However, these results indicate that there is a potential for further refinement to reduce the input impedance of these devices at these operating frequencies through optimisation of the SAW device geometry. This conclusion is drawn from the observation that measurements in Table 12 show a broad spread of performance characteristics. A comprehensive optimisation informed by these results will thus likely yield a more optimal device.

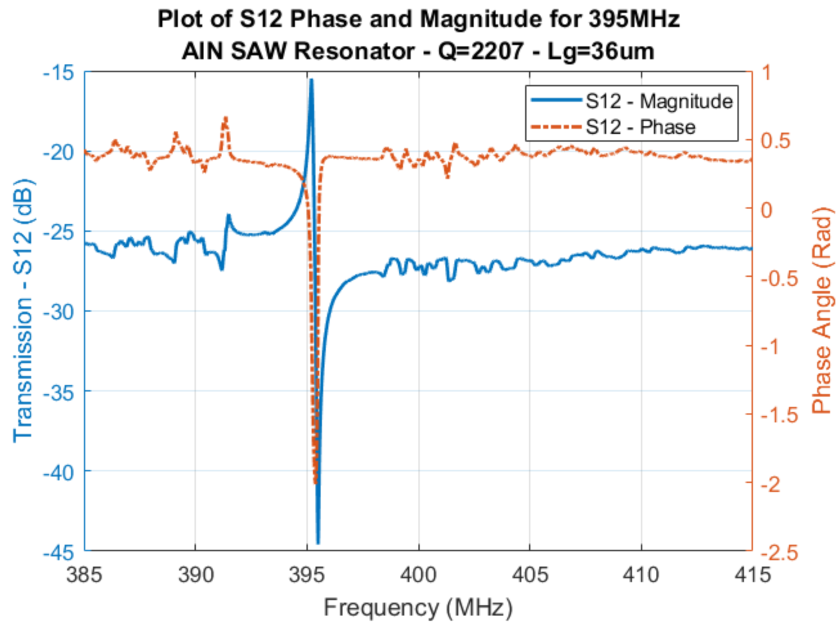

Figure 23: Plot of S12 scattering parameter magnitude and phase for a 395 MHz SAW resonator on AlN.

From the measured center frequency of these resonators the effective acoustic velocity of the resonator substrate including gold electrodes can be determined using:

$$\nu_m = f_0 \lambda \tag{33}$$

Thus for the 50 nm gold electrodes on 1 μm AlN, 100 nm molybdenum on silicon substrates used in this work the effective acoustic velocity can be calculated to be approximately $\nu_{m_{AlN}} = 4740\ m/s$ which is well in line with many commonly quoted ranges for AlN films, all-be-it on the low side [62]. However, given the use of gold electrodes with a low typical acoustic velocity of 3700 m/s this can be accounted for.

5.3.5 Peak Splitting Observed in SAW Devices

Peak splitting was observed in devices with large effective cavity lengths $L_{c_{eff}}$ with electrodes comprising gold on Ti. Figure 24 shows the S12 scattering parameter

for such a device. It is theorised that this results from additional resonate modes within the cavity due to increased cavity bandwidth.

The increase in cavity bandwidth can be related to the material selection made for the SAW electrodes. This conclusion is drawn from the observation of early devices where chrome was used as an adhesion layer for gold. These devices did not demonstrate any noticeable peak splitting even for large IDT separations $L_g = 36um$. However, the adhesion of chrome to AlN was not ideal, which necessitated a move to a titanium adhesion layer. For devices with a titanium adhesion layer, peak splitting is very noticeable, particularly for $Sc_{.37}Al_{.63}N$ devices where-in peak splitting can be seen in all devices with $L_g > 12\mu m$. Figure 19 shows the $S12$ parameter of a $Sc_{.37}Al_{.63}N$ device with $L_g = 36\mu m$ using chrome as an adhesion layer. As can be seen, no peak splitting is evident. Figure 24 however, shows clear peak splitting at otherwise identical operating and design conditions, with the exception of the use of titanium as an adhesion layer.

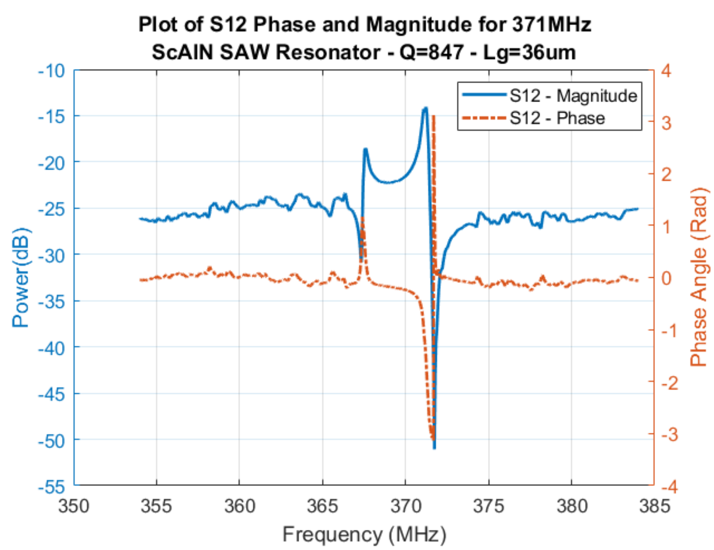

Figure 24: Peak splitting in S12 response of 371 MHz $Sc_{.37}Al_{.63}N$ SAW resonator with 200 reflectors and $L_g = 36\ \mu m$.

It can be shown that the cavity bandwidth of a SAW resonator is directly relatable to the reflectivity per grating by [63]:

$$\Delta f = \frac{2f_0|r_s|}{\pi} \tag{34}$$

As such, the use of the alternative adhesion layer with different mechanical properties would have varied the reflectivity of the individual reflector gratings. In the case of titanium, it has significantly lower density and Young's modulus when compared to chrome. This results in a more significant acoustic mis-match between the reflector arrays and the piezoelectric substrate increasing the magnitude of the reflections from each of the reflector gratings. An inspection of (34) shows that increasing reflectivity $|r_s|$ results in increased cavity bandwidth. From the cavity bandwidth the magnitude of the reflectivity of titanium and gold electrodes can be estimated via rearrangement of (34) as $|r_s| = 0.016$ for a measured cavity bandwidth of 3.7 MHz and center frequency $f_0 = 369.1$ MHz in Figure 24.

The observation that peak splitting is more prominent in $Sc_{.37}Al_{.63}N$ devices can be attributed to the lower measured acoustic velocity of the $Sc_{.37}Al_{.63}N$ devices. As observed in Sections 5.3.1 and 5.3.4 the acoustic velocity of the $Sc_{.37}Al_{.63}N$ substrate is measurably lower than that of the AlN substrate. Thus the gold on Ti electrodes represent a larger acoustic mismatch and thus higher bandwidth is achieved in the $Sc_{.37}Al_{.63}N$ SAW devices.

5.3.6 Comparison of SAW Performance with Split and Solid Electrodes

The solid electrode devices typically show lower performance vs. the split electrode designs as a result of self cancellation of the cavity due to reflections from the IDTs. Figure 25 shows a comparison of the S22 response for two different 369 MHz

and 371 MHz $Sc_{.37}Al_{.63}N$ SAW devices using split or solid electrode designs. This illustrates the clear superiority of the split electrode designs; with these devices showing $4-5$ times the the performance at resonance, as well as significantly higher Q factor. The measured BVD circuit parameters for these devices are presented in Table 13.

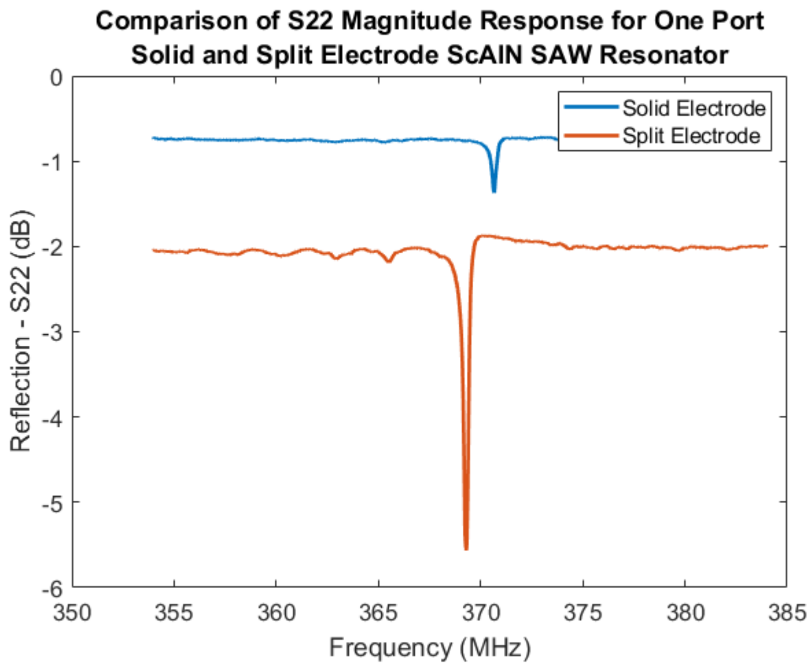

Figure 25: Comparison of S22 reflection for one port $Sc_{.37}Al_{.63}N$ SAW resonators with split and solid electrodes.

Table 13: Butterworth Van-Dyke equivalent circuit parameters for 1 port, split and solid electrode $Sc_{.37}Al_{.63}N$ SAW devices with gold electrodes.

f_0 (MHz)	R_m (Ω)	L_m (μH)	C_m (fF)	C_0 (pF)	Q	N_r	κ^2
369 Split	33.68	9	20.63	–	620	100	1.09%
369 Solid	93.59	8.02	22.98	–	–	100	0.36%

Given the clear performance benefits of split electrode designs, it is evident that they should be used wherever lithographic constraints allow for it.

5.3.7 Comparison of Piezoelectric Transducer Material Performance

As predicted, the $Sc_{.37}Al_{.63}N$ transducers vastly outperformed the AlN resonators in terms of motional impedance and electromechanical coupling due to the significantly higher piezoelectric coefficients reported for this material. Typically $Sc_{.37}Al_{.63}N$ resonators out performed AlN resonators in insertion loss by $1-5\ dB$. From Tables 11 and 12 it can be observed that polycrystalline $Sc_{.37}Al_{.63}N$ resonators did display typically lower Q than the AlN device tested in this work.

From related works, it is reasonable to conclude that additional film stress and abnormal grain growth due to the high scandium concentration in the films tested contributed to this reduction in Q [30, 57, 64]. Given this information, due consideration must be given to the trade off between insertion losses and electromechanical coupling with device Q factor.

However, it is also worth noting that $Sc_{.37}Al_{.63}N$ films are relatively immature compared to AlN films. Thus it is reasonable to suspect that part of the advantage seen in Q factor for the AlN films is a result of better developed deposition techniques. Further advancements in the deposition of single crystal films of $Sc_{.37}Al_{.63}N$ could see this gap close to some greater or lesser extent.

5.4 Vibrational Characterisation

A highly performing $Sc_{.37}Al_{.63}N$ SAW resonator was chosen to undergo vibrational testing. The device was mounted in 24 pin dual inline package (DIP) for vibrational testing and then fitted into the vibrational test fixture described in Section 4.2 of this work. Figure 26 shows the resulting plot of device resonant frequency f_0 at each vibrational frequency. Also shown at Figure 26 is a reduced data set with the standard deviation of each of the five measurements taken at each frequency. The number of data points has been reduced in this figure to aid in reading clarity.

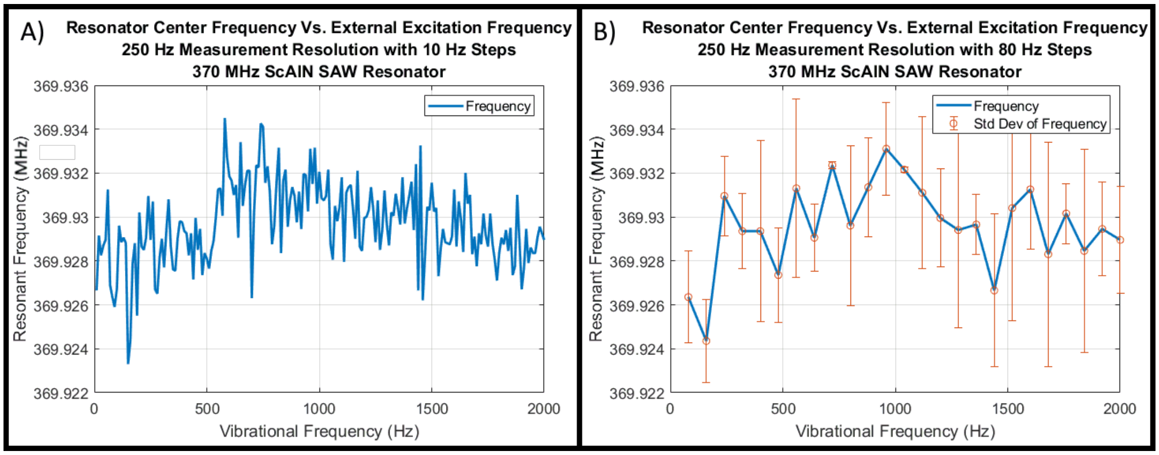

Figure 26: Plot of resonator center frequency in (MHz) for a 370 MHz $Sc_{.37}Al_{.63}N$ SAW resonator when under vibrational load from 0-2000 Hz. A) Full data set at 10 Hz steps; B) Reduced data set at 80 Hz steps showing standard deviation; the data has been reduced for reading clarity.

As can be observed from Figure 26 external vibrations do appear to result in minor variations in the center frequency of the tested $Sc_{.37}Al_{.63}N$ resonator. However, the standard deviation of the data indicates that there is significant variability within each of the five measurements taken at each vibrational frequency. This would appear to indicate that much of the apparent variation in the measured center frequency results from the noise in the measurements taken at each frequency and not from a change in the frequency of the resonator itself.

The maximum value for the standard deviation measured was $8.2KHz$. This would appear indicative of the external sources of noise as the measured frequency does not maintain a stable value even when the external excitation is maintained at a constant amplitude and frequency. This value for measurement standard deviation is also close to the total dynamic range of the measured data which is $11.2KHz$, this is again indicative of noise.

Measurement error in the network analyser as a source of variation seen in the data is considered unlikely. For the settings used during testing, the frequency accuracy of the network analyser was near $1Hz$ based on the manufacturer specification.

A possible source of these observed variation is noise induced via vibration of the RF cables [65]. Whilst efforts were taken to relieve strain from the cables and dampen any vibrations, some vibration of the cables is inevitable. However, from [65] it is known that such noise should be roughly be normally distributed. Figure 27 shows a histogram of the vibrational data. The mean of this distribution is centered at the mean operating frequency of the resonator when not externally excited (e.i. at $0Hz$ external vibration). This distribution bares a mild resemblance to a normal distribution with a relatively low skewness of 0.111 (by definition a normal distribution has a skewness of 0). The data appears to show a slight tendency towards higher frequencies with a kurtosis of 3.45 (kurtosis for a normal distribution is 3 by definition). The skewness of the data would indicate a slight tendency of the resonator center frequency to move towards higher frequencies under vibrational load.

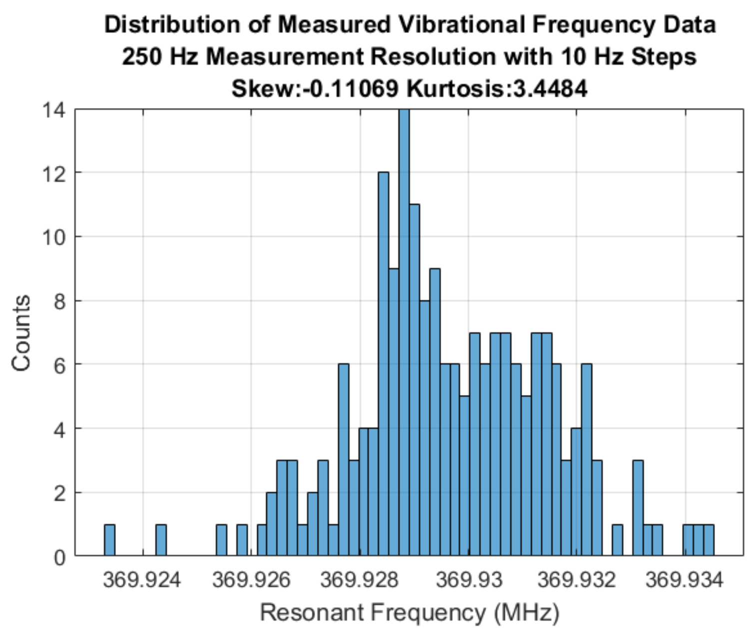

Figure 27: Histogram showing distribution of the 200 resonant frequency measurements taken. Values for the skewness and kurtosis of the data are also provided in the title

From these measurements it is suggested that the SAW resonators are relatively unaffected by external vibrations. With much of the observed variation in frequency

likely a result of the measurement noise and not a result of the resonator center frequency shifting due to the external vibration.

5.5 Etching of ScAlN and AlN Films

Multiple chemistries were investigated in this work for the etching of $Sc_{.37}Al_{.63}N$ films using both Cl_2 and fluorine based dry etch chemistries and a series of wet etches. Combinations of these chemistries were also investigate for both AlN and $Sc_{.37}Al_{.63}N$.

The reactive ion etching (RIE) chemistries investigate for $Sc_{.37}Al_{.63}N$ are shown in Table 14. As can be seen, there are no effective etches for $Sc_{.37}Al_{.63}N$ using fluorinated gasses and BCl_3. Some etches did demonstrate slight etching for samples chips taken from near the wafer edge up to 45 nm under the test 2 conditions. However, this etch was self limiting and did not exceed a depth of 45 nm. Samples closer to the wafer center showed no such etching under the conditions in test 2-4. It is assumed that the minor etching observed under the test 2 conditions may have resulted from a thin layer of lower quality film being etched. Given that these results were not repeatable, the etch rate is reported as zero. These results indicate that fluorinated dry etch chemistries as shown in tests 2-4 may be suitable for etching lower quality $Sc_{.37}Al_{.63}N$ films at low etch rates, but proved ineffective for the $Sc_{.37}Al_{.63}N$ films employed in this work.

Greater success was found in etching $Sc_{.37}Al_{.63}N$ films using BCl_3 and Cl_2 chemistries. Initial etch rates for the film were estimated at 50 $\mu m/min$. This value aligns with the etch rates observed in other works [39, 41]. However, these etch rates were only achievable to certain depths. Deeper etches appeared to become self limiting, resisting further RIE etching attempts. The depth at which this effect was observed varied between $200 - 500$ nm.

Table 14: RIE etch parameters attempted for $Sc_{.37}Al_{.63}N$ films. Whilst BCl_3 and Cl_2 RIE did consistently etch the $Sc_{.37}Al_{.63}N$ films, inconsistencies it the etch yielded an overall indeterminate etch rate.

Parameter	**Test 1**	**Test 2**	**Test 3**	**Test 4**	**Test 6**
RIE Power (W)	150	-	-	-	150
ICP Power (W)	300	400	600	600	300
Pressure (mTorr)	5	50	60	60	50
BCl_3 (sccm)	8	30	30	30	0
Cl_2 (sccm)	32	-	-	-	32
CF_4 (sccm)	-	10	-	-	-
SF_6 (sccm)	-	-	52	-	-
CHF_3 (sccm)	-	-	-	52	-
Etch Rate (nm/min)	Indeterminate	0	0	0	0

Hypothesises as to the root cause of the observed self limiting etch and a more in depth discussion are presented in Section 5.5.0.1.

The RIE etching chemistries investigate for AlN are shown in Table 15. Both Cl_2 and fluorine based etching chemistries show promising etch results with only a slight increase in etch rate for the more commonly used Cl_2 etch chemistry. However, the Cl_2 etch was conducted at significantly lower chamber pressure. This should in general yield a more isotropic etch profile. Given these promising results, a combination of these dry etch chemistries and wet etching was used in this work to etch AlN films dependant on equipment availability.

Table 15: RIE dry etch recipes tested for etching of AlN films in this work.

Parameter	**Test 1**	**Test 2**
RIE Power (W)	250	65
ICP Power (W)	-	300
Pressure (mTorr)	50	5
BCl_3 (sccm)	30	8
Cl_2 (sccm)	-	32
CF_4 (sccm)	10	-
SF_6 (sccm)	-	-
CHF_3 (sccm)	-	-
Etch Rate (nm/min)	45	50

5.5.0.1 Issues in the Development of Released Devices

Issues encountered in the etching of the $Sc_{.37}Al_{.63}N$ films used in this work, coupled with other delays prevented the full fabrication of the released WEM and LEM resonators and filters. Of particular note is the anomalous results encountered during RIE of the $Sc_{.37}Al_{.63}N$ films. Reviews of related literature indicated multiple workable etch recipes for this material exploiting chlorine based chemistries.

However, etch results from this work showed sporadic and inconsistent etch depths over a number of etch trials, regardless of the methods of preparation of the film. Table 16 shows a detailed selection of chlorine based etch results and etch rates for the $Sc_{.37}Al_{.63}N$ films studied in this work. Chlorine based etches were selected as they showed the greatest potential for etching $Sc_{.37}Al_{.63}N$ films as indicated in Table 14.

Table 16: RIE etch rates for a selection of $Sc_{.37}Al_{.63}N$ etches using chlorine based chemistries.

Trial	$\boldsymbol{Cl_2}$ ($sccm$)	$\boldsymbol{BCl_3}$ ($sccm$)	**RIE (W)**	**ICP (W)**	**P (mTorr)**	**rate (nm/min)**
1	32	8	65	300	5	5
2	32	8	150	300	5	50.1
3	32	8	150	300	5	18
4	32	8	150	300	5	8
5	32	8	150	300	5	9
6	32	8	150	300	5	0.0027 (re-etch)

These results show no consistent trend, and none were able to reach a suitable full depth etch of 1 μm. It is proposed that inconsistencies in the crystallography of the deposited film resulted in crystallographic etch stops within the $Sc_{.37}Al_{.63}N$ films.

This is supported by the apparent observation that the maximum etch depth achieved during RIE appeared to vary more strongly as a function of the location that samples were taken from within the test wafer than as a function of the etch time, with deeper etches achieved in specific regions of the wafer but not others. In

the case of the highest etch rate observed, which was trial 2, this corresponded to a sample taken from near the edge of the diced test wafer. Given that film uniformity is typically variable near the edge of a deposited wafer, it is not unreasonable to assume that this anomalously high etch rate may be due to a variation in the crystallographic properties of the film at this point. However, the location of chips on the wafer was not initially controlled for in this work, limiting the utility of these observations.

Adding further credence to the etch stop theory, trial 6 was an attempted re-etch of a sample previously etched to approximately 200 nm. This sample was etched for 88 min under the conditions listed in Table 16. However, no significant increase in the etch depth could be detected. This is in spite of the results from previous etches, such as trial 5, indicating that an etch rate of $8 - 18$ nm/min should be expected for the operating conditions used. This demonstrates that the etch recipe previously used in trials 4 and 5 was ineffective at etching the $Sc_{.37}Al_{.63}N$ film past 200 nm etch depth. These results appear strongly indicative of some form of interfering etch stop layer within the deposited $Sc_{.37}Al_{.63}N$ films.

5.5.1 Wet KOH Etching of AlN and ScAlN Thin Films

A wet etch for AlN was developed in this work utilising 20% potassium hydroxide (KOH) in deionised water at room temperature. Etching of $Sc_{.37}Al_{.63}N$ films was attempted with this KOH wet etch, but the resulting etch was very poor with lateral etching dominating. This resulted in an affect more akin to cratering of the $Sc_{.37}Al_{.63}N$ surface.

Characterisation of the etch showed rapid etching of AlN and slow etching of $Sc_{0.37}Al_{0.63}N$ films. The use of KOH as an etchant required the selection of a very tenacious photoresist due to the aggressive etching properties and highly alkaline PH of KOH solutions. Su-8 5 negative photoresist was prepared for KOH etching as

shown in Table 17 and Table 18. Hard baking of the film was necessary in order to yield sufficient film adhesion and resistance to the KOH solution. After etching the Su-8 film was striped using O_2 plasma.

Table 17: Su-8 5 spin parameters for wet KOH etch of $Sc_{.37}Al_{.63}N$ and AlN

Thickness	**3 μm**	**5 μm**
Spread Speed (rpm)	500	500
Spread Time (s)	10	10
Spin Speed (rpm)	3000	2000
Spin Time (s)	60	60

Table 18: Su-8 bake, exposure, development and hard bake parameters

Thickness	**3 μm**	**5 μm**
Pre-bake	65°C 2min	65°C 2min
Soft Bake	95°C 5min	95°C 5min
Exposure	60 mj/cm^2	85 mj/cm^2
Post Exposure pre-Bake	65°C 2min	65°C 2min
Post Exposure Hard Bake	95°C 1min	95°C 1min
Developer	1 min	1 min
Hard Bake	200°C 5min	200°C 5min

Several etch characterisations were conducted yielding the results shown in Table 19. As can be see the etch rate for AlN is quite high at approximately 300 nm/min, the etch rate for $Sc_{.37}Al_{.63}N$ films however, was significantly lower and the resulting etch very rough. Thus whilst etching of $Sc_{.37}Al_{.63}N$ films using the 20% KOH solution investigated in this work is possible, issues with the ability of the Su-8 mask to survive prolonged exposures in the KOH solution and the poor quality of the etch were found to be limiting.

The etch profile of AlN piezoelectric etched in KOH was found to depend strongly on whether the Su-8 film was hard-baked or not. Excessive undercut was noted for etches were the photoresist was not hard-baked. This appears to result from the Su-8

Table 19: KOH room temperature wet etch results for $Sc_{.37}Al_{.63}N$ and AlN

Material	$\boldsymbol{Sc_{0.37}Al_{0.63}N}$	**AlN**
KOH (% w/w)	20	20
Temperature ($^{\circ}C$)	20	20
Etch rate (nm/min)	25	300

film losing adhesion around the etch site exposing additional AlN to the enchant and is not a result of purely lateral etching. Thus it is strongly recommended that Su-8 films be hard baked for KOH etching. Figure 28 shows a comparison of two etches conducted on AlN using hard baked and non-hard-baked Su-8 films. The features shown are 50 μm squares.

The etch profile for the hard baked film is well developed and crisp. Where-as for the non-hard-baked film there is significant degradation of the etch profile. In both cases the etching was conducted in 1 μm AlN to a full depth of 1 μm

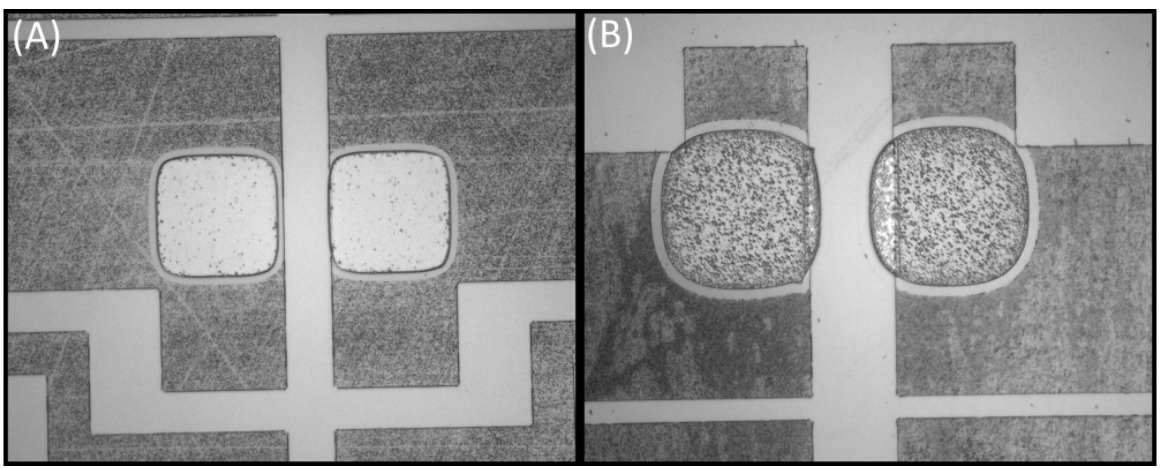

Figure 28: Comparison of etch profile for hard-baked and non-hardbake Su-8 films on AlN using KOH. The features shown are 50 μm squares on the mask. A) Etch profile for hard-baked Su-8 film; B) Etch profile for un-baked Su-8 film

5.5.2 Other Wet Etch Attempts

Several additional photoresist developers were trialed as potential wet etchants for $Sc_{.37}Al_{.63}N$ films in order to determine other possible candidates for etching this material. These included MF-26A (active ingredient TMAH) heated to $60°C$, SU-8 developer (active ingredient 2-methoxy-1-methylethyl acetate) heated to $60°C$, and 351 developer (active ingredient $NaOH$) heated to $60°C$. Each developer was used undiluted and the samples were masked using Su-8 5 as discussed in Section 5.5.1 for KOH etching. Whilst each of these chemicals is a strong base, and known to etch AlN, none showed any potential for etching the $Sc_{.37}Al_{.63}N$ films used in this work under the conditions described.

5.6 Recommendations

The SAW devices developed in this work show potential for high performance near the 2 GHz frequency bands of interest to this research. It has been demonstrated that the effects of external vibrations are relatively minor, although ultimately whether this is acceptable will be application specific. It has also been shown that the $Sc_{.37}Al_{.63}N$ SAW devices developed are very resilient to external electric fields with minimal impact to the operation point of the devices even when subjected to significant field strengths. The clear performance benefits of split transducer designs have also been illustrated and low insertion losses are observable for the device tested in this work.

From these results it is recommended that $Sc_{.37}Al_{.63}N$ SAW devices would likely be suitable candidates for operation in space based environments. Devices could be readily developed with electron beam lithography to achieve the lithographic resolution required for operation near 2 Ghz. Further refinement of the deposition of $Sc_{.37}Al_{.63}N$ and in particular, the use of single crystal $Sc_{.37}Al_{.63}N$ should also yield improved Q factor for these devices. Recent works also indicate that the growth of

single crystal $Sc_{.37}Al_{.63}N$ on silicon carbide may yield good results [45]. This has the added benefit that silicon carbide has a very high Akhiezer limit, increasing the potential upper limit on device performance.

SAW resonator designs should also leverage split transducers to minimise losses from self cancellation. The ratio of film thickness to wavelength should be given careful consideration. From the results of this work it appears that the ratio of film thickness to wavelength should meet the values recommend by Lin Shu et al. [55].

VI. Conclusion

This work has demonstrated through experimental measurements the enhanced performance of scandium aluminum nitride ($Sc_XAl_{1-X}N$) when compared to aluminum nitride (AlN); with significantly lower insertion loss and higher bandwidth notable. For the 37% scandium aluminum nitride ($Sc_{.37}Al_{.63}N$) films investigate in this work it has been shown that resonators manufactured from these thin films are resistant to external vibration and electric fields. However, the $Sc_{.37}Al_{.63}N$ films did show lower Q factor when compared to similar AlN devices. It has been concluded that this likely results from additional film stress and abnormal grain growth associated with the high scandium concentration. It is hoped however that future improvements in $Sc_XAl_{1-X}N$ deposition methods may mitigate these issues, with single crystalline $Sc_XAl_{1-X}N$ films being particularly promising.

Molybdenum electrodes show promise for use with $Sc_XAl_{1-X}N$ films allowing for high quality piezoelectric growth, low losses, and high temperature resistance. Molybdenum also poses a low environmental risk and is CMOS compatible. However, difficulties encountered in deposition of sufficiently high quality films in this work limited its use. Results from this work also conclude that titanium nitride (TiN) is likely an unsuitable material for high temperature electrodes due to high RF losses and sheet resistance values.

Limitations encountered in this work prevented the development of suitable resonators and filters for operation at L-band frequencies. However the materials, techniques and methods employed in this work all show promise for future efforts to develop such devices.

6.1 Future Work

Future work in the application of $Sc_XAl_{1-X}N$ piezoelectric to space based roles could include:

- Determine root cause for inconsistent reactive ion etching (RIE) of $Sc_{.37}Al_{.63}N$ films encounter in this work.

- Experiment with thicker (near 1 μm) single crystalline films of $Sc_XAl_{1-X}N$ and electron beam lithography to develop high frequency layouts for surface acoustic wave (SAW) devices on single crystal $Sc_XAl_{1-X}N$ operating near 2 GHz. Improved lithographic techniques will allow for the implementation of more effective transducer designs such as split electrode transducers at the scale required to excite these frequencies. Ideally these devices will show Q factors close to, or exceeding that of AlN.

- Investigate the suitability of $Sc_XAl_{1-X}N$ films for high temperature use and thermal cycle life due to concerns regarding film stress and abnormal grain growth resulting from high scandium concentrations.

- An investigation the effects of varied scandium concentrations on the robustness and vibrational resistance of $Sc_XAl_{1-X}N$ resonators should also be considered.

- Use the SAW, width extensional mode (WEM), and length extensional mode (LEM) topologies identified in this work to develop resonators and filters operating near 2 GHz for space based roles.

Bibliography

1. R. Aigner, J. Ella, H.-J. Timme, L. Elbrecht, W. Nessler, and S. Marksteiner. Advancement of MEMS into RF-filter applications. In *Digest. International Electron Devices Meeting,*, pages 897–900. IEEE, 2002.

2. Yunhong Hou, Meng Zhang, Guowei Han, Chaowei Si, Yongmei Zhao, and Jin Ning. A review: aluminum nitride MEMS contour-mode resonator. *Journal of Semiconductors*, 37(10):101001, oct 2016.

3. Chao Yu Chen, Ming Huang Li, and Sheng Shian Li. CMOS-MEMS Resonators and Oscillators : A Review. *Sensors and Materials*, 30(4):733, 2018.

4. Roberto Sorrentino, Luca Pelliccia, and Simone Bastioli. Recent progress in miniaturized and reconfigurable filters for advanced communications and space applications. In *2011 MICROWAVES, RADAR AND REMOTE SENSING SYMPOSIUM*, pages 20–23. IEEE, aug 2011.

5. Shirin Ghaffari, Saurabh A. Chandorkar, Shasha Wang, Eldwin J. Ng, Chae H. Ahn, Vu Hong, Yushi Yang, and Thomas W. Kenny. Quantum Limit of Quality Factor in Silicon Micro and Nano Mechanical Resonators. *Scientific Reports*, 3(1):3244, dec 2013.

6. Gayathri Pillai and Sheng-shian Li. Piezoelectric MEMS Resonators: A Review. *IEEE Sensors Journal*, XX(XX):1–1, 2020.

7. Farrokh Ayazi, Benoit Hamelin, and Jeremy Yang. Nano-Precision Deep Reactive Ion Etching of Monocrystalline 4H-SiCOI for Bulk Acoustic Wave Resonators with Ultra-Low Dissipation. *ECS Transactions*, 97(4):3–13, may 2020.

8. T. Ibn-Mohammed, I.M. Reaney, S.C.L. Koh, A. Acquaye, D.C. Sinclair, C.A. Randall, F.H. Abubakar, L. Smith, G. Schileo, and L. Ozawa-Meida. Life cycle assessment and environmental profile evaluation of lead-free piezoelectrics in comparison with lead zirconate titanate. *Journal of the European Ceramic Society*, 38(15):4922–4938, dec 2018.

9. Morito Akiyama, Toshihiro Kamohara, Kazuhiko Kano, Akihiko Teshigahara, Yukihiro Takeuchi, and Nobuaki Kawahara. Enhancement of Piezoelectric Response in Scandium Aluminum Nitride Alloy Thin Films Prepared by Dual Reactive Cosputtering. *Advanced Materials*, 21(5):593–596, feb 2009.

10. T. Ibn-Mohammed, S. C. L. Koh, I. M. Reaney, D. C. Sinclair, K. B. Mustapha, A. Acquaye, and D. Wang. Are lead-free piezoelectrics more environmentally friendly? *MRS Communications*, 7(1):1–7, mar 2017.

11. Gabriel Giribaldi, Luca Colombo, Fabio Bersano, Cristian Cassella, and Matteo Rinaldi. Investigation on the Impact of Scandium-doping on the kt2 of ScxAl1-xN Cross-sectional Lamé Mode Resonators. In *2020 IEEE International Ultrasonics Symposium (IUS)*, pages 1–4. IEEE, sep 2020.

12. Hengky Chandrahalim. *Voltage Tunable Radio Frequency Microelectromechanical Resonators And Filters*. Phd, Cornell University, 2009.

13. Ali Kourani, Ruochen Lu, and Songbin Gong. A Wideband Oscillator Exploiting Multiple Resonances in Lithium Niobate MEMS Resonator. *IEEE Transactions on Ultrasonics, Ferroelectrics, and Frequency Control*, 67(9):1854–1866, sep 2020.

14. Shweta Humad, Reza Abdolvand, G.K. Ho, Gianluca Piazza, and Farrokh Ayazi. High frequency micromechanical piezo-on-silicon block resonators. In *IEEE In-*

ternational Electron Devices Meeting 2003, volume 00, pages 39.3.1–39.3.4. IEEE, 2003.

15. Reza Abdolvand, Behraad Bahreyni, Joshua Lee, and Frederic Nabki. Micromachined Resonators: A Review. *Micromachines*, 7(9):160, sep 2016.

16. Dimitra Psychogiou, Roberto Gomez-Garcia, and Dimitrios Peroulis. Tunable acoustic-wave-lumped-element resonator (awlr)-based bandpass filters. In *2016 IEEE MTT-S International Microwave Symposium (IMS)*, volume 2016-Augus, pages 1–4. IEEE, may 2016.

17. Le Yan, Jian Wu, and W.C. Tang. A 1.14 GHz piezoelectrically transduced disk resonator. In *18th IEEE International Conference on Micro Electro Mechanical Systems, 2005. MEMS 2005.*, pages 203–206. IEEE, 2005.

18. Gabrielle D. Vukasin, Veronica K. Sanchez, Janna Glaze, Nicholas E. Bousse, Nathan Bissel, Dongsuk D. Shin, Hyun-Keun Kwon, David Heinz, Ernest T.-T. Yen, and Thomas W. Kenny. Anchor Design Affects Dominant Energy Loss Mechanism in a Lamé Mode MEM Resonator. *Journal of Microelectromechanical Systems*, 29(5):860–866, oct 2020.

19. Anosh Daruwalla, Haoran Wen, Chang-Shun Liu, and Farrokh Ayazi. Low motional impedance distributed Lamé mode resonators for high frequency timing applications. *Microsystems & Nanoengineering*, 6(1):53, dec 2020.

20. Muhammad Wajih Ullah Siddiqi and Joshua E.Y. Lee. Wide acoustic bandgap solid disk-shaped phononic crystal anchoring boundaries for enhancing quality factor in AlN-on-Si MEMS resonators. *Micromachines*, 9(8):1–12, 2018.

21. L Yan, W Pang, J Wu, William Chi-Keung Tang, and E.-S. Kim. High frequency micromechanical piezo actuated disk resonator. *Solid-State Sensor, Actuator and Microsystems Workshop*, pages 372 – 375, 2004.

22. T.L. Sounart, T.A. Michalske, and K.R. Zavadil. Frequency-dependent electrostatic actuation in microfluidic MEMS. *Journal of Microelectromechanical Systems*, 14(1):125–133, feb 2005.

23. American National Standards Institute (Organization/Institution). An American National Standard: IEEE Standard on Piezoelectricity. *IEEE Transactions on Sonics and Ultrasonics*, 31(2):8–10, mar 1984.

24. Chih Hao Lee, Fong Gang Guo, and Chia Chin Chu. The Thickness Dependent of Optical Properties, Resistance, Strain and Morphology of Mo Thin Films for The Back Contact of CIGS Solar Cells. *Chinese Journal of Physics*, 50(2):311–321, 2012.

25. Micheal Burke, Alan Blake, Ian M. Povey, Michael Schmidt, Nikolay Petkov, Patrick Carolan, and Aidan J. Quinn. Low sheet resistance titanium nitride films by low-temperature plasma-enhanced atomic layer deposition using design of experiments methodology. *Journal of Vacuum Science & Technology A: Vacuum, Surfaces, and Films*, 32(3):031506, may 2014.

26. Filiz Keleş, Yavuz Atasoy, and Ayşe Seyhan. Sputtered Mo-bilayer thin films with reduced thickness and improved electrical resistivity. *Materials Research Express*, 6(12):126455, feb 2020.

27. Subhash M. Pandharkar, Sachin R. Rondiya, Avinash V. Rokade, Bharat B. Gabhale, Habib M. Pathan, and Sandesh R. Jadkar. Synthesis and characterization

of molybdenum back contact using direct current-magnetron sputtering for thin film solar cells. *Frontiers in Materials*, 5(March):1–6, 2018.

28. Ravinder S. Dahiya and Maurizio Valle. *Robotic Tactile Sensing*. Springer Netherlands, Dordrecht, 2013.

29. Stefan Mertin, Vladimir Pashchenko, Fazel Parsapour, Clemens Nyffeler, Cosmin S. Sandu, Bernd Heinz, Oliver Rattunde, Gabriel Christmann, Marc-Alexandre Dubois, and Paul Muralt. Enhanced piezoelectric properties of c-axis textured aluminium scandium nitride thin films with high scandium content: Influence of intrinsic stress and sputtering parameters. In *2017 IEEE International Ultrasonics Symposium (IUS)*, pages 1–4. IEEE, sep 2017.

30. Stefan Mertin, Bernd Heinz, Oliver Rattunde, Gabriel Christmann, Marc-Alexandre Dubois, Sylvain Nicolay, and Paul Muralt. Piezoelectric and structural properties of c-axis textured aluminium scandium nitride thin films up to high scandium content. *Surface and Coatings Technology*, 343(January):2–6, jun 2018.

31. Miguel A. Caro, Siyuan Zhang, Markku Ylilammi, Tommi Riekkinen, Michelle A. Moram, Olga Lopez-Acevedo, Jyrki Molarius, and Tomi Laurila. Piezoelectric coefficients and spontaneous polarization of ScAlN (2015 J. Phys. Condens. Matter 27 245901). *Journal of Physics: Condensed Matter*, 27(27):279602, jul 2015.

32. Jiri Fialka and Petr Benes. Comparison of methods of piezoelectric coefficient measurement. In *2012 IEEE International Instrumentation and Measurement Technology Conference Proceedings*, pages 37–42. IEEE, may 2012.

33. Hiroyoshi Momida and Tamio Oguchi. Effects of lattice parameters on piezoelectric constants in wurtzite materials: A theoretical study using first-principles and statistical-learning methods. *Applied Physics Express*, 11(4):041201, apr 2018.

34. Nathan Jackson. Influence of silicon crystal orientation on piezoelectric textured aluminium nitride deposited on metal electrodes. *Vacuum*, 132:47–52, oct 2016.

35. Guofeng Chen and Matteo Rinaldi. Aluminum Nitride Combined Overtone Resonators for the 5G High Frequency Bands. *Journal of Microelectromechanical Systems*, 29(2):148–159, apr 2020.

36. K. Eldred; WM. Hoberts; R. White. Structural Vibrations in Space Vehicals. Technical report, Aeronautical Systems Division Air Force Systems Command, Dayton, Ohio, 1961.

37. George C. Marshall space Flight Center (Organization/Institution). Vibration and acoustic analyses, Saturn SA-10 flight. Technical report, George C. Marshall space Flight Center, Huntsville, Alabama, 1965.

38. A. Lucibello, G. Capoccia, E. Proietti, R. Marcelli, B. Margesin, V. Mulloni, F. Giacomozzi, F. Vitulli, M. Scipioni, and G. Bartolucci. Reliable response of RF MEMS LTCC packaged switches after mechanical and thermal stress. In *2014 Symposium on Design, Test, Integration and Packaging of MEMS/MOEMS (DTIP)*, number April, pages 1–5. IEEE, apr 2014.

39. Luca Colombo, Abhay Kochhar, Changting Xu, Gianluca Piazza, Sergey Mishin, and Yury Oshmyansky. Investigation of 20% Scandium-doped Aluminum Nitride films for MEMS laterally vibrating resonators. In *2017 IEEE International Ultrasonics Symposium (IUS)*, pages 1–1. IEEE, sep 2017.

40. Yao Zhu, Nan Wang, Gengli Chua, Chengliang Sun, Navab Singh, and Yuandong Gu. ScAlN-Based LCAT Mode Resonators Above 2 GHz With High FOM and Reduced Fabrication Complexity. *IEEE Electron Device Letters*, 38(10):1481–1484, oct 2017.

41. Qi Wang, Yipeng Lu, Sergey Mishin, Yury Oshmyansky, and David A. Horsley. Design, Fabrication, and Characterization of Scandium Aluminum Nitride-Based Piezoelectric Micromachined Ultrasonic Transducers. *Journal of Microelectromechanical Systems*, 26(5):1132–1139, oct 2017.

42. Vladimir Pashchenko, Ramin Matloub, Fazel Parsapourkolour, Paul Muralt, Sylvain Ballandras, and Ken Haffner. Hybrid BAW/SAW AlN and AlScN thin film resonator. In *2016 IEEE International Ultrasonics Symposium (IUS)*, volume 2016-Novem, pages 1–4. IEEE, sep 2016.

43. Roy H. Olsson, Zichen Tang, and Michael D'Agati. Doping of Aluminum Nitride and the Impact on Thin Film Piezoelectric and Ferroelectric Device Performance. In *2020 IEEE Custom Integrated Circuits Conference (CICC)*, pages 1–6. IEEE, mar 2020.

44. Zeji Chen, Xiao Kan, Quan Yuan, Tianyun Wang, Jinling Yang, and Fuhua Yang. A Switchable High-Performance RF-MEMS Resonator with Flexible Frequency Generations. *Scientific Reports*, 10(1):4795, dec 2020.

45. Afzaal Qamar, Hoang-Phuong Phan, Toan Dinh, Nam-Trung Nguyen, and Mina Rais-Zadeh. ScAlN/3C-SiC/Si platform for monolithic integration of highly sensitive piezoelectric and piezoresistive devices. *Applied Physics Letters*, 116(13):132902, mar 2020.

46. Sarah Shahraini, Hakhamanesh Mansoorzare, Amirreza Mahigir, and Reza Abdolvand. Thickness-Lamé Thin-Film Piezoelectric-on-Silicon Resonators. *Journal of Microelectromechanical Systems*, 29(3):296–305, jun 2020.

47. Chien-Hao Weng, Gayathri Pillai, and Sheng-Shian Li. A Thin-Film Piezoelectric-on-Silicon MEMS Oscillator for Mass Sensing Applications. *IEEE Sensors Journal*, 20(13):7001–7009, jul 2020.

48. Yanbo He, Bichoy Bahr, Mengwei Si, Peide Ye, and Dana Weinstein. A tunable ferroelectric based unreleased RF resonator. *Microsystems & Nanoengineering*, 6(1):8, dec 2020.

49. Nan Wang, Yao Zhu, Bangtao Chen, and Ying Zhang. Over 12% of Coupling Coefficient Demonstrated by 3GHz Sc 0.12 Al 0.88 N Based Laterally Coupled Alternating Thickness (LCAT) Mode Resonators. In *2019 IEEE International Ultrasonics Symposium (IUS)*, volume 2019-Octob, pages 1971–1973, Glasgow, oct 2019. IEEE.

50. Michael Schneider, Mario DeMiguel-Ramos, Andrew J. Flewitt, Enrique Iborra, and Ulrich Schmid. Scandium Aluminium Nitride-Based Film Bulk Acoustic Resonators. In *Proceedings*, volume 1, page 305. MDPI, aug 2017.

51. Dixiong Wang, Jeffrey Zheng, Pariasadat Musavigharavi, Wanlin Zhu, Alexandre C Foucher, Susan E. Trolier-McKinstry, Eric A Stach, and Roy H. Olsson. Ferroelectric Switching in Sub-20 nm Aluminum Scandium Nitride Thin Films. *IEEE Electron Device Letters*, 41(12):1774–1777, dec 2020.

52. Mingyo Park, Zhijian Hao, Rytis Dargis, Andrew Clark, and Azadeh Ansari. Epitaxial Aluminum Scandium Nitride Super High Frequency Acoustic Resonators. *Journal of Microelectromechanical Systems*, 29(4):490–498, aug 2020.

53. Zachary A. Schaffer, Gianluca Piazza, Sergey Mishin, and Yury Oshmyansky. Super High Frequency Simple Process Flow Cross-Sectional Lamé Mode Resonators in 20% Scandium-Doped Aluminum Nitride. In *2020 IEEE 33rd International*

Conference on Micro Electro Mechanical Systems (MEMS), pages 1281–1284. IEEE, jan 2020.

54. Supriyo Datta. *Surface Acoustic Wave Devices.* Prentice Hall, Englewood Cliffs, 1986.

55. Lin Shu, Bin Peng, Chuan Li, Dongdong Gong, Zhengbing Yang, Xingzhao Liu, and Wanli Zhang. The Characterization of Surface Acoustic Wave Devices Based on AlN-Metal Structures. *Sensors*, 16(4):526, apr 2016.

56. Zhijian Hao, Mingyo Park, Dea Gyu Kim, Andrew Clark, Rytis Dargis, Haoshen Zhu, and Azadeh Ansari. Single Crystalline ScAlN Surface Acoustic Wave Resonators with Large Figure of Merit (Q $\times$ kˆ2). In *2019 IEEE MTT-S International Microwave Symposium (IMS)*, volume 2019-June, pages 786–789. IEEE, jun 2019.

57. Gabriel Giribaldi, Luca Colombo, Fabio Bersano, Cristian Cassella, and Matteo Rinaldi. Investigation on the Impact of Scandium-doping on the kt2 of ScxAl1-xN Cross-sectional Lamé Mode Resonators. In *2020 IEEE International Ultrasonics Symposium (IUS)*, pages 1–4. IEEE, sep 2020.

58. Afzaal Qamar, Savannah R. Eisner, Debbie G. Senesky, and Mina Rais-Zadeh. Ultra-High-Q Gallium Nitride SAW Resonators for Applications With Extreme Temperature Swings. *Journal of Microelectromechanical Systems*, 29(5):900–905, oct 2020.

59. M. P. Larsson, R R A Syms, and A. G. Wojcik. Improved adhesion in hybrid Si-polymer MEMS via micromechanical interlocking. *Journal of Micromechanics and Microengineering*, 15(11):2074–2082, nov 2005.

60. T.G. Brown. Harsh military environments and microelectromechanical (MEMS) devices. In *Proceedings of IEEE Sensors 2003 (IEEE Cat. No.03CH37498)*, volume 2, pages 753–760. IEEE, 2003.

61. Asseko Ondo Jean Claude, Blampain Eloi Jean Jacques, N'tchayi Mbourou Gaston, Traore Ndama Adoum, Obame Ndong Elysée, and Elmazria Omar. Modeling and Electrical Characterization of a Bilayer Pt/AlN/Sapphire One Port Resonator for Sensor Applications. *Electronics*, 10(4):370, feb 2021.

62. Aamir F. Malik, Varun Jeoti, Mohamad Fawzy, Asif Iqbal, Zubair Aslam, Mohanraj Soundara Pandian, and Eloi Marigo. Estimation of SAW velocity and coupling coefficient in multilayered piezo-substrates AlN/SiO/Si. In *2016 6th International Conference on Intelligent and Advanced Systems (ICIAS)*, pages 1–5. IEEE, aug 2016.

63. Gianfranco Avitabile, Luca Roselli, Carlo Atzeni, and Gianfranco Manes. *Surface acoustic wave resonators*. Maters, University of Milan, 2013.

64. Chen Liu, Bangtao Chen, Minghua Li, Yao Zhu, and Nan Wang. Evaluation of the Impact of Abnormally Orientated Grains on the Performance of ScAlN-based Laterally Coupled Alternating Thickness (LCAT) Mode Resonators and Lamb Wave Mode Resonators. In *2020 IEEE International Ultrasonics Symposium (IUS)*, pages 1–3. IEEE, sep 2020.

65. Archita Hati, Craig W. Nelson, and David A. Howe. Vibration-induced PM and AM noise in microwave components. *IEEE Transactions on Ultrasonics, Ferroelectrics, and Frequency Control*, 56(10):2050–2059, oct 2009.

Acronyms

$Sc_{.37}Al_{.63}N$ 37% scandium aluminum nitride. iv, vii, viii, ix, x, 3, 4, 33, 34, 37, 38, 43, 45, 46, 59, 60, 61, 62, 63, 67, 68, 69, 70, 71, 73, 74, 75, 76, 77, 78, 79, 80, 81, 82, 1

$Sc_{.3}Al_{.7}N$ scandium aluminum nitride. viii, 33, 64, 65

$Sc_XAl_{1-X}N$ scandium aluminum nitride. iv, 5, 6, 14, 16, 18, 19, 21, 22, 23, 24, 25, 26, 27, 28, 34, 38, 39, 41, 59, 81, 82, 1

AFRL Air Force Research Laboratory. 45, 47

AlN aluminum nitride. iv, vii, viii, ix, x, 16, 21, 22, 24, 33, 34, 37, 40, 41, 42, 43, 44, 45, 48, 59, 64, 65, 66, 68, 70, 73, 74, 76, 77, 78, 79, 81, 82, 1

BAW bulk acoustic wave. 10

BVD Butterworth Van-Dyke. 50, 51, 60, 64, 69

DIP dual inline package. 52, 70

FeRAM Ferroelectric RAM. 25

FOM figure of merit. 8, 9, 65

GPIB General Purpose Interface Bus. 53, 54

HF hydrofluoric acid. 43, 45, 46

IDT interdigital transducer. viii, 28, 29, 31, 32, 36, 37, 40, 41, 61, 62, 67, 68

KOH potassium hydroxide. viii, x, 41, 42, 43, 44, 45, 46, 47, 48, 76, 77, 78

LEM length extensional mode. iv, 2, 3, 35, 36, 58, 63, 75, 82, 1

LOBAR lateral overtone bulk acoustic resonator. 26

LTCC Low Temperature Co-Fired Ceramic. 21

MEMS microelectromechanical systems. iv, 1, 2, 4, 5, 6, 7, 8, 9, 11, 14, 15, 16, 18, 19, 20, 21, 23, 24, 25, 26, 27, 48, 1

NA network analyser. 54

NASA National Air and Space Agency. 20

PZT lead zirconate titanate. 2, 3

RF radio frequency. 1, 2, 4, 5, 7, 8, 9, 11, 12, 14, 20, 21, 23, 25, 58

RIE reactive ion etching. x, 43, 44, 45, 46, 73, 74, 75, 82

SAED selective area electron diffraction. 18

SAW surface acoustic wave. iv, vii, 2, 3, 5, 10, 14, 24, 28, 29, 30, 31, 32, 34, 39, 40, 45, 57, 58, 59, 60, 61, 62, 64, 65, 67, 68, 69, 70, 79, 82, 1

SEM scanning electron microscope. 4, 61

SiN silicon nitride. 44

TiN titanium nitride. iv, 3, 4, 14, 24, 45, 58, 59, 81

TPoS thin film piezoelectric on silicon. 3

TPOS thin film piezoelectric on silicon. 19

WEM width extensional mode. iv, vii, 2, 3, 35, 36, 37, 38, 58, 63, 75, 82, 1

REPORT DOCUMENTATION PAGE

Form Approved OMB No. 0704–0188

1. REPORT DATE *(DD–MM–YYYY)*	2. REPORT TYPE	3. DATES COVERED *(From — To)*
08–03–2020	Master's Thesis	Sept 2019 — Mar 2021

4. TITLE AND SUBTITLE

ROBUST SCANDIUM ALUMINUM NITRIDE MEMS RESONATORS FOR L
BAND OPERATION IN ORBITAL ENVIRONMENTS

5a. CONTRACT NUMBER

5b. GRANT NUMBER

5c. PROGRAM ELEMENT NUMBER

6. AUTHOR(S)

Israel W. Dunk

5d. PROJECT NUMBER

5e. TASK NUMBER

5f. WORK UNIT NUMBER

7. PERFORMING ORGANIZATION NAME(S) AND ADDRESS(ES)

Air Force Institute of Technology
Graduate School of Engineering and Management (AFIT/EN)
2950 Hobson Way
WPAFB OH 45433-7765

8. PERFORMING ORGANIZATION REPORT NUMBER

AFIT-ENG-MS-21-M-029

9. SPONSORING / MONITORING AGENCY NAME(S) AND ADDRESS(ES)

AFRL/RV
Air Force Research Laboratory's Space Vehicles Directorate
Kirtland Air Force Base NM 87123
Email: madeleine.naudeau@us.af.mil

10. SPONSOR/MONITOR'S ACRONYM(S)

AFRL/RV

11. SPONSOR/MONITOR'S REPORT NUMBER(S)

12. DISTRIBUTION / AVAILABILITY STATEMENT

DISTRIBUTION STATEMENT A:
APPROVED FOR PUBLIC RELEASE; DISTRIBUTION UNLIMITED.

13. SUPPLEMENTARY NOTES

14. ABSTRACT

This thesis investigates AlN alloyed with scandium in a variety of resonator architectures including WEM, overtone WEM, LEM, and SAW that have the potential to achieve high levels of electrical performance and environmental robustness. SAW resonators operating near $370\ MHz$ are fabricated on polycrystalline $Sc_{.37}Al_{.63}N$, and AlN with the resulting devices compared and conclusions drawn as to the merits of each material. The design and fabrication of SAW devices is discussed in detail, with the operating characteristics of these resonators then tested both electrically and mechanically. Mechanical characterisation includes analysis of vibration and shock effects on the fabricated devices. The electrical characterisation in this work studies the electrical equivalent parameters of the resonators produced. A study is also made into the feasibility of resonant frequency tuning for $Sc_XAl_{1-X}N$ SAW resonators using DC bias voltages. The devices produced in this work show the future potential for $Sc_XAl_{1-X}N$ piezoelectric materials to produce MEMS resonators operating at high frequencies, with high resilience to shocks, external electric fields and vibrations.

15. SUBJECT TERMS

Scandium Aluminum Nitride, SAW, WEM, Vibration, Frequency Tuning

16. SECURITY CLASSIFICATION OF: a. REPORT	b. ABSTRACT	c. THIS PAGE	17. LIMITATION OF ABSTRACT	18. NUMBER OF PAGES	19a. NAME OF RESPONSIBLE PERSON
U	U	U	UU	107	Flight Lieutenant Israel W. Dunk, AFIT/ENG
					19b. TELEPHONE NUMBER *(include area code)* N/A, ext N/A; Israel.Dunk@defence.gov.au